Ab initio Path Integral Molecular Dynamics: Theory and Application

Dissertation
zur Erlangung des Grades
"Doktor rerum naturalium"
(Dr. rer. nat)
an der Universität Paderborn
Fakultät für Naturwissenschaften
von

Dipl.-Phys.
Thomas Spura

Paderborn, 2015

Die vorliegende Arbeit wurde in der Zeit von Januar 2013 bis April 2014 am Institut für Physikalische Chemie der Johannes Gutenberg-Universität Mainz sowie von Mai 2014 bis September 2015 am Institut für Technische Chemie der Universität Paderborn in der Arbeitsgruppe von Prof. Dr. Thomas D. Kühne angefertigt.

Prüfungskommission

Vorsitzender:	Prof. Dr.-Ing. Hans-Joachim Warnecke
Erstgutachter:	Prof. Dr. Thomas D. Kühne
Zweitgutachter:	Jun. Prof. Dr. Simone Sanna
Beisitzer:	PD Dr. Hans Egold
Tag der Einreichung:	17.09.2015
Tag der mündlichen Prüfung:	22.10.2015

Ab Initio Path Integral Molecular Dynamics: Theory and Application

Thomas Spura

ABSTRACT

Atomistic systems containing light atoms at low temperatures can be described with Path integral molecular dynamics (PIMD). In the present work, new, highly accurate simulation techniques in this field were developed. Thereby, the required interatomic potential is calculated with coupled cluster theory (CC), which is the current state of the science.

As an highly accurate theory is usually accompanied with significant computational demands, the aim of the present work was furthermore to reduce the computational cost of both techniques — the CC calculation and the PIMD simulation. The calculation of the interatomic potential in the molecular dynamics simulation is accelerated by providing initial guesses to several iterative equations in CC theory that approximate their final solution.

New methods to reduce the computational demands of the PIMD simulation are presented that exploit further properties of the interatomic potential. These techniques are applied to the CC-based PIMD simulations, but can also be used with general analytic interatomic potentials. They are especially beneficial for systems with light particles and low temperatures and therefore performed with hydrogen-bonded systems. As a result of these investigations, the slightest perturbations to the molecular electronic structure is investigated by inspecting the highly sensitive nuclear magnetic resonance parameters and this simulation technique can now be used for small molecules at finite temperature on a routine basis.

Ab Initio Path Integral Molecular Dynamics: Theory and Application

Thomas Spura

ZUSAMMENFASSUNG

Atomare Systeme mit leichten Atomen bei geringen Temperaturen können mit der Pfad-Integral-Molekulardynamik (PIMD) beschrieben werden. Im Rahmen dieser Arbeit wurden neue Simulationstechniken auf diesem Gebiet entwickelt. Die dabei notwendigen interatomaren Potentiale werden gemäß des aktuellen Stands der Wissenschaft mit der Coupled-Cluster-Theorie (CC) berechnet.

Da eine hoch genaue Theorie üblicherweise mit signifikanten Anforderungen an die Rechenleistung einhergeht, war ein weiteres Ziel dieser Arbeit diesen rechnerischen Aufwand von beiden Theorien zu reduzieren — der CC-Rechnung und der PIMD-Simulation. Die Berechnung des interatomaren Potentials in der Molekulardynamik-Simulation wird beschleunigt, indem die Startwerte mehrerer iterativer Gleichungen der CC-Theorie so gewählt werden, dass sie der finalen Lösung bereits sehr nahe sind.

Neue Methoden zur Reduktion des Rechenaufwandes der PIMD-Simulation werden vorgestellt, die weitere Eigenschaften des interatomaren Potentials ausnutzen. Diese Methoden werden in dieser Arbeit mit der CC-basierten PIMD-Simulation angewandt, es können jedoch auch andere analytische Potential hierbei verwendet werden. Diese neuen Simulationstechniken sind besonders nützlich bei Systemen mit leichten Atomen und niedrigen Temperaturen und werden daher bei Wasserstoff gebundenen Systemen angewandt. Die kleinsten Störungen der molekularen Elektronenstruktur werden durch die Berechnung von sehr empfindlichen NMR-Parameter sichtbar gemacht. Diese Simulationstechnik kann von nun an bei kleinen Molekülen bei endlicher Temperatur routinemäßig durchgeführt werden.

CONTENTS

NOMENCLATURE

$\beta = 1/(k_B T)$	inverse temperature
$\Gamma(t)$	point in phase space Γ at time t
K	predictor length of the Always Stable Predictor
M	total number of time steps
N	number of particles
N_c	order of the Taylor polynomial for the contraction scheme with derivatives
N_e	number of electrons in the system
P	number of beads of the ring polymer
$T_{jj'}$	transformation matrix from bead system with j' beads to bead system with j beads
$\mathbf{p}(t)$	momenta of a system with N particles $\mathbf{p}(t) = \{\mathbf{p}_1(t), \ldots, \mathbf{p}_N(t)\}$ or momenta of all $N \times P$ particles in the PIMD case $\mathbf{p}(t) = \{\mathbf{p}_1^{(1)}(t), \ldots, \mathbf{p}_N^{(P)}(t)\}$
$\mathbf{x}(t)$	positions of a system with N particles $\mathbf{x}(t) = \{\mathbf{x}_1(t), \ldots, \mathbf{x}_N(t)\}$ or positions of all $N \times P$ particles in the PIMD case $\mathbf{x}(t) = \{\mathbf{x}_1^{(1)}(t), \ldots, \mathbf{x}_N^{(P)}(t)\}$
$\mathbf{x}_i^{(j)}$	positions of the j-th bead of particle i
$\mathbf{x}^{(c)}$	centroid or center of mass of the ring polymer
$\hat{\Lambda}$	de-excitation operator
$\hat{T}$	cluster operator

Part I

INTRODUCTION

1

OVERVIEW

EVERYTHING in our surrounding physical world consists of atoms whose dynamics can be studied microscopically with molecular dynamics by simulating the accurate movement of the atoms. Richard P. Feynman once put this as "The world is a dynamic mess — of jiggling things." [1]. For systems containing light atoms at low temperatures, nuclear quantum effects (NQE) such as quantum mechanical zero-point energy and tunneling effects play a crucial role. They are required to describe the correct quantitative and qualitative behavior of these systems and must be taken into account. *Ab initio* path integral molecular dynamics (AI-PIMD) [2–10], where no results from experiments are included in the parameters of the theory, has been shown to explain and predict various physical phenomena [11–28]. These calculations where the interatomic potential is computed "on-the-fly" based on density functional theory [29, 30] are accompanied by significant computational demands. Even though "DFT can be used to describe all of chemistry, biochemistry, biology, nanosystems and materials" as Becke, the author of one of the most cited papers of all time once put it [31], it is very desirable to calculate the interactions as accurate as possible. For instance, when describing hydrogen-bonded systems, even the tiniest energetic interaction must be taken into account [32–36] because even a small error of 0.2 kcal/mol corresponds to a temperature difference at which water freezes or evaporates [37]. In quantum chemistry, electron correlation is incorporated in a systematic way [38, 39] by using coupled cluster (CC) theory to calculate interatomic interactions in a highly accurate fashion [39–42].

This work combines coupled cluster with path integral molecular dynamics to the computationally very demanding CC-PIMD, which will also be christened *quantum molecular dynamics* in this thesis. Moreover, new methods are developed to accelerate these calculations so that these simulations can be routinely applied.

This work is structured as follows: In the next chapter, the fundamental ideas of path integral molecular dynamics and coupled cluster as well as the underlying Hartree-Fock theory are introduced. In Part II, the coupled cluster theory is combined with path integral molecular dynamics to *quantum molecular dynamics*. Furthermore, efficient methods to accelerate the calculation of the CC-based interaction potential are presented. The main idea of these methods is to find a good initial guess for the iterative electronic structure equations to accelerate their convergence. The Hartree-Fock part of the calculation is accelerated by using the old molecular orbitals to estimate the initial guess to the iterative equations. This approach is inspired by the second generation Car-Parrinello approach of Kühne *et al.* [43, 44] and has been published in Ref. [37]. We would like to note in passing that this is to the best of our knowledge the first MD simulation at the CC level of theory and the first CC-based *ab initio*-PIMD simulation ever realized. To reduce the computational cost of these computationally very demanding calculations, the knowledge of the previous amplitudes of the CC calculations is used to reduce the computational cost of the dominating solution of the so-called cluster and $\hat{\Lambda}$ amplitudes. In Part III, new methods to speed up general PIMD calculations are derived that exploit further properties of the physical nature of the interatomic potential such as separability into different time and spatial domains or derivability. Thereby, the standard ring contraction scheme [45, 46] is extended to exploit further properties of the interatomic potential. In Chapter 5, the potential energy surface is approximated with a lower level of theory. Computational time is invested to calculate the difference between both theories. This will reduce the computational demands while still sampling the potential energy surface of the computational more demanding theory. An alternative route to approximate the potential energy surface is given in Chapter 6, where further derivatives are included in the ring contraction scheme. This approach is independent of the knowledge of an approximate lower level of theory and can be carried out straightforwardly for any analytic interatomic potential.

The following publications are part of this thesis and are included in Chapters 3–6 of this thesis:

1. T. Spura, H. Elgabarty, and T. D. Kühne, *"On-the-fly" coupled cluster path-integral molecular dynamics: Impact of nuclear quantum effects on the protonated water dimer*, *Phys. Chem. Chem. Phys.*, **17**, 14355 (2015)

2. T. Spura, H. Elgabarty, and T. D. Kühne, *Accelerated "on-the-fly" coupled cluster path-integral molecular dynamics: Impact of nuclear quantum effects on an asymmetric proton*, *in preparation* (2015)

3. T. Spura, H. Elgabarty, and T. D. Kühne, *Quantum ring contraction scheme with a delta potential: Impact of nuclear quantum effects on* H_5^+, *in preparation* (2015)

4. T. Spura and T. D. Kühne, *Quantum ring contraction scheme with derivatives*, *in preparation* (2015)

Further publications, which have been published while carrying out this thesis or will be published in the near future are

5. M. Doemer, T. Spura, R. Z. Khaliullin, and T. D. Kuehne, *Tetrahedral, when in fluid state*, *Nachr. Chem.*, **61**, 1203 (2013)

6. T. Spura, C. John, S. Habershon, and T. D. Kühne, *Nuclear quantum effects in liquid water from path-integral simulations using an ab initio force-matching approach*, *Mol. Phys.*, **113**, 808 (2014)

7. J. Kessler, H. Elgabarty, T. Spura, K. Karhan, P. Partovi-Azar, A. A. Hassanali, and T. D. Kühne, *Structure and dynamics of the instantaneous water/vapor interface revisited by path-integral and ab initio molecular dynamics simulations*, *J. Phys. Chem. B*, **119**, 10079 (2015)

8. T. Spura, P. Virnau, and T. D. Kühne, *High precision estimates of liquid-vapor critical points for water-salt mixtures*, *in preparation* (2015)

9. A. Köster, T. Spura, G. Rutkai, H. Wiebeler, T. D. Kühne, and J. Vrabec, *Thermodynamic properties of force-matched water force fields*, *in preparation* (2015)

10. H. Wiebeler, T. Spura, and T. D. Kühne, *Nuclear quantum effects in liquid water with three body corrected, path integral simulations*, *in preparation* (2015)

11. C. John, T. Spura, J. Kessler, S. Habershon, and T. D. Kühne, *An auxillary potential ring-polymer contraction scheme for path integral molecular dynamics simulations*, *in preparation* (2015)

2

THEORETICAL FOUNDATIONS OF QUANTUM MOLECULAR DYNAMICS

In this chapter, the basic theories are presented that are either unified in the presented coupled cluster-based path integral molecular dynamics simulation or are used to develop new methods to increase the applicability thereof in Part II. This combination of coupled cluster (that solves the electronic Schrödinger equation) and the path integral molecular dynamics simulation (that solves the nuclear Schrödinger equation) is christened as *quantum molecular dynamics*. At first, a general introduction into molecular dynamics is given with a derivation of one of the most common integrators that is extended in the path integral case soon thereafter. Both simulation approaches require an interatomic potential to describe the interactions between particles. When this interaction can be split into different contributions with different time scales the multiple time step algorithm improves the computational efficiency of the molecular dynamics simulations. When this interaction can be furthermore decomposed into different spatial contributions, the ring polymer contraction scheme outlined next speeds up the calculation of the interatomic potential in the path integral case. These schemes form the basis for new methods to accelerate PIMD simulations later on in Part III. The interatomic potential depends directly on the positions of the nuclei and therefore implicitly on the time. It is evaluated on the coupled cluster level of theory, which belongs to the class of the so-called post-Hartree-Fock theory, because it uses the Hartree-Fock theory as a foundation. The basic principles of both theories close this introductory chapter.

2.1 MOLECULAR DYNAMICS

The fundamental laws of classical mechanics were originally used to predict the motions of planets and are applied in molecular dynamics (MD) to study the motion of microscopical systems [57]. The associated equations of motions are solved with numerical methods as in general it is not possible to carry out an analytic solution. An accurate numerical integrator is key in the field of MD and one of the most common integrators — the velocity Verlet integrator — is derived in the following with the help of the Liouville formalism.

2.1.1 *Liouville Formalism*

In this section, the Liouville formalism by Tuckerman *et al.* [58] to generate arbitrary integrators is presented for the case of the velocity Verlet integrator [59, 60]. Within this formalism it is straightforward to derive time reversible integration schemes, which are more complex, but computationally less demanding.

The full set of positions of an N particle system at time t are denoted as a shorthand with $\mathbf{x}(t) = \{\mathbf{x}_1(t), \ldots, \mathbf{x}_N(t)\}$ and the full set of momenta as $\mathbf{p}(t) = \{\mathbf{p}_1(t), \ldots, \mathbf{p}_N(t)\}$. Initially at starting time t, the system is at the point in phase space $\Gamma(t) = \Gamma(\mathbf{x}(t), \mathbf{p}(t))$. The time derivative of $\Gamma(t)$ defines the Liouville operator iL [61]

$$\frac{d\Gamma}{dt} = \sum_{j=1}^{N} \left(\dot{\mathbf{x}}_j \frac{\partial \Gamma}{\partial \mathbf{x}_j} + \mathbf{F}_j \frac{\partial \Gamma}{\partial \mathbf{p}_j} \right) \tag{2.1}$$

$$= \underbrace{\sum_{j=1}^{N} \left(\dot{\mathbf{x}}_j \frac{\partial}{\partial \mathbf{x}_j} + \mathbf{F}_j \frac{\partial}{\partial \mathbf{p}_j} \right)}_{iL} \Gamma, \tag{2.2}$$

where $\dot{\mathbf{x}}_j$ denotes the velocity of the j-th particle and $\mathbf{F}_j = -\nabla_{\mathbf{x}_j} V(\mathbf{x})$ is the force originating the interatomic potential between the particles acting on particle j. Integrating this differential equation, one obtains the propagator $e^{iL\Delta T}$

$$\Gamma(t + \Delta T) = e^{iL\Delta T} \Gamma(t), \tag{2.3}$$

that propagates the system from the initial point in phase space $\Gamma(t)$ to a point at a later time $t + \Delta T$. The system will then be located at the final point in phase

space $\Gamma(t+\Delta T) = \Gamma(\mathbf{x}(t+\Delta T), \mathbf{p}(t+\Delta T))$. As this operator consists of two non-commuting operators iL_x and iL_p [57]

$$iL = \underbrace{\sum_{j=1}^{N} \dot{x}_j \frac{\partial}{\partial x_j}}_{iL_x} + \underbrace{\sum_{j=1}^{N} F_j \frac{\partial}{\partial p_j}}_{iL_p}, \tag{2.4}$$

the classical propagator $e^{iL_x+iL_p}$ cannot be simply split into $e^{iL_x}e^{iL_p}$. Instead, for two non-commuting operators A and B, i.e. $[A,B] \neq 0$, the Trotter theorem states [62–64]

$$e^{(A+B)\Delta T} = \lim_{M\to\infty} \left(e^{B\Delta T/2M} e^{A\Delta T/M} e^{B\Delta T/2M}\right)^M. \tag{2.5}$$

Applying this theorem to Eq. 2.4 leads to a time reversible integrator [57]

$$\begin{aligned} e^{iL\Delta T} = e^{(iL_x+iL_p)\Delta T} &= \lim_{M\to\infty} \left(e^{iL_p\Delta T/2M} e^{iL_x\Delta T/M} e^{iL_p\Delta T/2M}\right)^M \\ &= \lim_{M\to\infty} \left(e^{iL_p\Delta t/2} e^{iL_x\Delta t} e^{iL_p\Delta t/2}\right)^M, \end{aligned} \tag{2.6}$$

where the smaller time step $\Delta t = \Delta T/M$ is a small fraction of the total time difference ΔT. This formula immediately shows how to integrate the equations of motions to move the system from time t to a later time $t+\Delta T$ by M intermediate points in the phase space, each separated by the time Δt as depicted in Fig. 2.1. As an operator $e^{c\frac{\partial}{\partial x}}$ acts on a function $g(x)$ as [57]

$$e^{c\frac{\partial}{\partial x}} g(x) = g(x+c), \tag{2.7}$$

the instructions to integrate one small time step Δt is derived from Eq. 2.6 as

$$\begin{aligned} e^{iL_p\Delta t/2}\Gamma(\mathbf{x}(t), \mathbf{p}(t)) &= \Gamma(\mathbf{x} &&, \mathbf{p} + \mathbf{F}\Delta t/2) \\ &= \Gamma(\mathbf{x}(t) &&, \mathbf{p}(t+\Delta t/2)) && (2.8) \\ e^{iL_x\Delta t}\Gamma(\mathbf{x}(t), \mathbf{p}(t+\Delta t/2)) &= \Gamma(\mathbf{x} + \dot{\mathbf{x}}\Delta t &&, \mathbf{p}) \\ &= \Gamma(\mathbf{x}(t) &&, \mathbf{p}(t+\Delta t/2)) && (2.9) \\ e^{iL_p\Delta t/2}\Gamma(\mathbf{x}(t+\Delta t), \mathbf{p}(t+\Delta t)) &= \Gamma(\mathbf{x} &&, \mathbf{p} + \mathbf{F}\Delta t/2) \\ &= \Gamma(\mathbf{x}(t+\Delta t), \mathbf{p}(t+\Delta t)). && (2.10) \end{aligned}$$

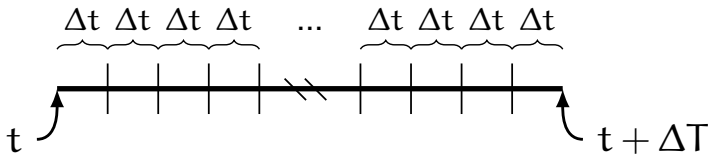

Figure 2.1: Example of a time bar from time t to a later time $t + \Delta T$, where each time step is separated by $\Delta t = \Delta T/M$.

This can also be written as

$$\mathbf{p}(t + \Delta t/2) = \mathbf{p}(t) + \frac{\Delta t}{2}\mathbf{F}(\mathbf{x}(t)) \tag{2.11}$$

$$\mathbf{x}(t + \Delta t) = \mathbf{x}(t) + \Delta t\, \dot{\mathbf{x}}(t + \Delta t/2) \tag{2.12}$$

$$\mathbf{p}(t + \Delta t) = \mathbf{p}(t + \Delta t/2) + \frac{\Delta t}{2}\mathbf{F}(\mathbf{x}(t + \Delta t)), \tag{2.13}$$

which is the three-step version of the velocity Verlet algorithm [57, 59] that is frequently used as integrator in MD. In the first step, the momenta are adjusted to the first half of the time step $t \to t + \Delta t/2$ as a result of forces acting on the particles. Then, the positions are moved to the full time step $t \to t + \Delta t$. After a force calculation at the new positions, finally also the momenta are adjusted to the next full time step $t \to t + \Delta t/2$ and the next integration step can be carried out. This way the positions and momenta are consistently moved from one time step to the next one until the total time frame $\Delta T = M\Delta t$ is reached after M integration steps. For M total time steps to move the system from time t to time $t + \Delta T$, this algorithm looks in Python pseudo code as

```
1 for i in range(ΔT/Δt): # Loop over M = ΔT/Δt total time steps
2     p = p + F · Δt/2
3     x = x + v · Δt
4     F = calculate_force(x) # Recalculate force at new positions x
5     p = p + F · Δt/2
```

Code 2.1: Python pseudocode that describes the instructions to move the system from time t to time $t + \Delta T$ with the velocity Verlet algorithm

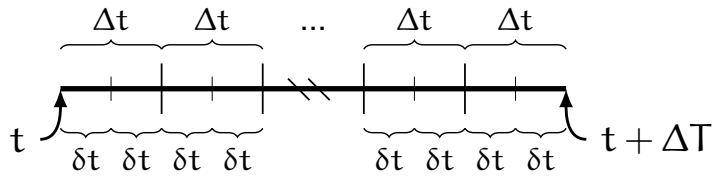

Figure 2.2: Example of a time bar with MTS employed from time t to a later time $t + \Delta T$, where each time step is separated by $\Delta t = \Delta T/M$. Each time step Δt consists of n_{mts} smaller time steps δt.

2.1.2 *Multiple Time Step Integrator*

The central idea of a multiple time step integrator (MTS) is to decompose the total interatomic interaction into (several) parts with different time scales and to propagate each interaction with the respective time step. The Liouville operator for the force iL_p in Eq. 2.4 is now reformulated as a sum of a fast varying $\mathbf{F}^F$ and a slowly varying contribution $\mathbf{F}^S$ of the total force [58, 65–68]

$$\begin{aligned} iL &= iL_x + iL_p^F + iL_p^S \\ &= \sum_{j=1}^{N} \dot{\mathbf{x}}_j \frac{\partial}{\partial \mathbf{x}_j} + \sum_{j=1}^{N} \mathbf{F}_j^F \frac{\partial}{\partial \mathbf{p}_j} + \sum_{j=1}^{N} \mathbf{F}_j^S \frac{\partial}{\partial \mathbf{p}_j}. \end{aligned} \tag{2.14}$$

A smaller time step that represents the time scale of the fast varying interaction $\delta t = \Delta t/n_{mts}$ is introduced and the Liouville operator with multiple time steps is obtained using the Trotter theorem from Eq. 2.5 as

$$e^{iL\Delta t} = e^{iL_p^S \Delta t/2} \left(e^{iL_p^F \delta t/2} e^{iL_x \delta t} e^{iL_p^F \delta t/2} \right)^{n_{mts}} e^{iL_p^S \Delta t/2}. \tag{2.15}$$

The time scale of the slow varying force is now described as multiple of the fast varying one. In Fig. 2.2 it is shown for the case of $n_{mts} = 2$ that for each time step of the slow varying interaction Δt two interactions of the fast varying interaction need to be calculated. This is especially helpful, if the slow varying interaction is computationally much more demanding than the fast one. When the latter is more or less of negligible computational complexity, a speed-up of n_{mts} is obtained.

The inner loop over n_{mts} of Eq. 2.15 is the same as the velocity Verlet algorithm from the previous chapter. The only changes are at the beginning and at the end of one integration step, the contribution of the slowly varying interaction acts on the

particles. For $M = \Delta T/\Delta t$ total time steps to move the system from time t to time $t + \Delta T$, this algorithm looks in Python pseudo code as

```
for i in range(ΔT/Δt): # Loop over M = ΔT/Δt total time steps
    p = p + F_slow · Δt/2
    for j in range(Δt/δt): # Loop over n_mts = Δt/δt
                           # multiple time steps
        p = p + F_fast · δt/2
        x = x + v · δt
        F_fast = calculate_fast_force(x) # Recalculate fast
                                         # varying force at
                                         # new positions x
        p = p + F_fast · δt/2
    F_slow = calculate_slow_force(x) # Recalculate slowly varying
                                     # force at new positions x
    p = p + F_slow · Δt/2
```

Code 2.2: Python pseudocode that describes the instructions to move the system from time t to time $t + \Delta T$ with the MTS algorithm

2.2 PATH INTEGRAL MOLECULAR DYNAMICS

Especially for systems with light atoms, nuclear quantum effects such as zero point energy and tunneling effects play a crucial role due to atomic delocalization. These effects become even more apparent with decreasing temperatures but it has been shown that they must be taken into account for water even at room temperature [51]. One possibility to incorporate nuclear quantum effects into the simulation is the path integral molecular dynamics (PIMD) formalism [2–5, 69, 70], where there is an isomorphism to replace the exact quantum partition function with classical harmonic P-bead polymers as shown in Fig. 2.3. This allows to calculate exact canonical quantum-mechanical properties by simulating P times the classical system in question and the exact canonical quantum partition function $Z(\beta)$ is recovered in the limit of $P \to \infty$ [3]

$$Z(\beta) = \mathrm{Tr}\left[\hat{\rho}(\beta)\right] = \mathrm{Tr}\left[e^{-\beta\hat{H}}\right] = \mathrm{Tr}\left[\left(e^{-\frac{\beta}{P}\hat{H}}\right)^{P}\right] = \lim_{P\to\infty} Z_P(\beta), \tag{2.16}$$

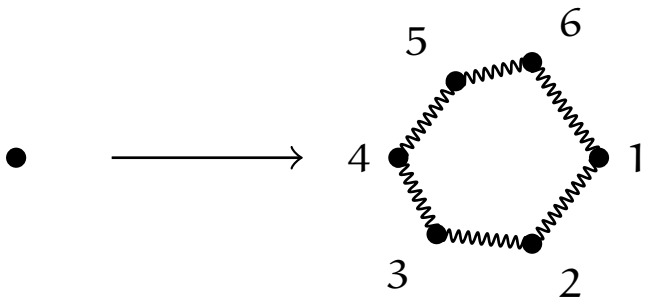

Figure 2.3: In the path integral formalism, a quantum particle is replaced by a P-bead ring polymer. This picture depicts the replacement with a 6-bead ring polymer.

where $\hat{\rho}(\beta)$ denotes the density matrix and $\beta = 1/(k_B T)$ is the inverse temperature. It should be noted that there is an important relation of the density matrix to the quantum mechanical time evolution operator $\hat{U}(t) = e^{-i\hat{H}t/\hbar}$, namely

$$\hat{\rho}(\beta) = \hat{U}(-i\beta\hbar). \tag{2.17}$$

Because of this relation the density matrix can be considered as an evolution operator in *imaginary* time $t = -i\hbar\beta$ [71]. The P-bead approximation of the partition function can be written after a derivation over inserting $P-1$ position eigenstates (for more details see e.g. Ref. [72]) as [4, 70, 72]

$$Z_P(\beta) = \left(\frac{1}{2\pi\hbar}\right)^{NP} \int d^{NP}\mathbf{x} \int d^{NP}\mathbf{p}\; e^{-\frac{\beta}{P} H_P(\mathbf{x},\mathbf{p})}. \tag{2.18}$$

In contrast to the classical case from Sec. 2.1, where $\mathbf{x}$ and $\mathbf{p}$ denoted the positions and momenta of N particles, they denote instead the positions and momenta of all $N \times P$ particles in all beads in the PIMD case. This path integral partition function converges at a finite number of beads P to the exact quantum partition function. The bead-Hamiltonian H_P that describes the iteratomic interactions between the particles and the intraatomic harmonic springs is given by

$$\begin{aligned} H_P(\mathbf{x},\mathbf{p}) = \sum_{j=1}^{P} \Bigg[\sum_{i=1}^{N} \frac{\mathbf{p}_i^{(j)2}}{2m_i} + \frac{m_i \omega_P^2}{2} \left(\mathbf{x}_i^{(j)} - \mathbf{x}_i^{(j+1)}\right)^2 \\ + V(\mathbf{x}_1^{(j)}, \ldots, \mathbf{x}_N^{(j)}) \Bigg], \end{aligned} \tag{2.19}$$

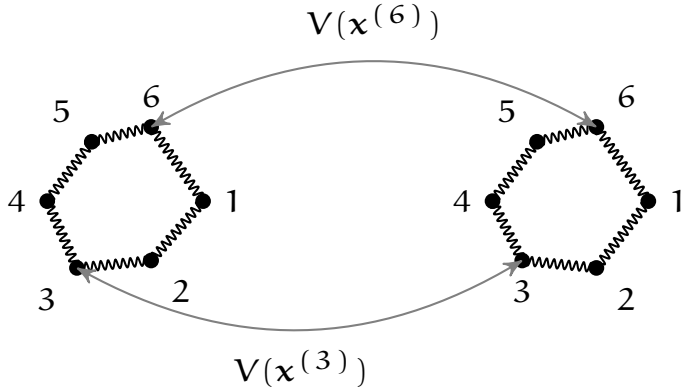

Figure 2.4: Example of a quantum system consisting of two particles denoted by two ring polymers with 6 beads each. Only particles with the same bead index j interact via the interatomic potential V, which is denoted exemplary for beads $P = 3$ and $P = 6$.

where m_i is the mass of the i-th particle and the frequency of the harmonic spring potential between adjacent beads is given by $\omega_P = P/(\beta\hbar)$. A subscript denotes the particle number and a superscript marks the bead number, so that $\boldsymbol{x}_i^{(j)}$ denotes the coordinates of the j-th bead of particle i. As each of the N ring polymers represents a closed path, $\boldsymbol{x}_i^{(j)}$ and $\boldsymbol{x}_i^{(j+P)}$ both denote the coordinates of the j-th bead of particle i. The interatomic potential $V(\boldsymbol{x}_1^{(k)}, \ldots, \boldsymbol{x}_N^{(k)})$, where $k \in \{1, \ldots, P\}$ is evaluated separately in each of the P bead systems, which is indicated for the case of $P = 6$ in Fig. 2.4. In this work, the potential will be evaluated on the Hartree-Fock or Coupled Cluster level of theory. Both theories are briefly outlined in Secs. 2.3 and 2.4 respectively. In this naïve but straightforward implementation of PIMD, the interatomic potential now needs to be evaluated P times instead of once in a conventional MD simulation. Even though these independent potential evaluations can be carried out in parallel, the computational demands still increase by the factor of P. This computational drawback can be reduced by exploiting some properties of this interatomic potential, such as the splitting of the interatomic potential into different time scales with the MTS scheme from the previous section or in different spatial contributions with the ring polymer contraction scheme outlined in the next section.

2.2.1 *Ring Polymer Contraction Scheme*

In analogy to the splitting of the interatomic potential into different contributions with different time scales as described in Sec. 2.1.2, the decomposition into different spatial contributions is discussed in this section. If the interatomic potential can be decomposed into a slowly varying long range and a fast varying short range contribution, the slowly varying potential can now be approximated on a smaller, contracted ring polymer with P' beads. The computational efficiency is now dramatically increased when the slowly varying potential is computational much more demanding than the fast varying potential. When the computational less demanding potential is of negligible computational complexity, this approach results in the ideal speed-up of P/P'. This idea has been used in the so-called ring polymer contraction scheme by Markland *et al.* [45, 46]. With this approach the ring polymer with P beads is efficiently transformed into one with P' beads via a detour over the normal mode representation. The transformation matrix $\mathcal{C}_{jk}^{(P)}$ that diagonalizes the harmonic spring terms in Eq. 2.19 and transforms the positions into normal mode representation is given by

$$\mathcal{C}_{jk}^{(P)} = \begin{cases} 1, & k = 0 \\ \sqrt{2}\cos(2\pi jk/P), & 0 < k < P/2 \\ \sqrt{2}\sin(2\pi jk/P), & P/2 < k < P \end{cases} \tag{2.20}$$

for the case if P is odd and when P is even the transformation matrix is given by

$$\mathcal{C}_{jk}^{(P)} = \begin{cases} 1, & k = 0 \\ \sqrt{2}\cos(2\pi jk/P), & 0 < k < P/2 \\ (-1)^P, & k = P/2 \\ \sqrt{2}\sin(2\pi jk/P), & P/2 < k < P \end{cases}. \tag{2.21}$$

The net transformation of the positions from the P-bead system to the positions of the contracted P'-bead system is now carried out with the following matrix multiplication

$$\mathbf{x}_i^{(j')} = \sum_{j=1}^{P} T_{j'j}\mathbf{x}_i^{(j)}, \tag{2.22}$$

where the transformation matrix $T_{j'j}$ consists of a normal mode and an inverse normal mode transformation

$$T_{j'j} = \frac{1}{P} \sum_{k=-l'}^{l'} \mathcal{C}_{j'k}^{(P')} \mathcal{C}_{jk}^{(P)}. \tag{2.23}$$

When $P' = P$ this transformation maps the ring polymer to itself and leaves it fully unchanged. For the case of $P' = 1$, the ring polymer is reduced to the center of mass or centroid of the system $\mathbf{x}^{(c)}$

$$\begin{aligned} \mathbf{x}_i^{(c)} &= \sum_{j=1}^{P} T_{1j} \mathbf{x}_i^{(j)} \\ &= \frac{1}{P} \sum_{j=1}^{P} \mathbf{x}_i^{(j)}, \end{aligned} \tag{2.24}$$

which is used in the further development of the ring polymer contraction scheme in Chapter 6. In this standard ring polymer contraction scheme however, this transformation is applied to approximate the slowly varying contribution V^S to the full potential V of the Hamiltonian in Eq. 2.19 with

$$\sum_{j=1}^{P} V^S(\mathbf{x}^{(j)}) = \frac{P}{P'} \sum_{j'=1}^{P'} V^S(\mathbf{x}^{(j')}). \tag{2.25}$$

This means that the potential on the right hand side is evaluated on a smaller ring polymer with P' beads. The force on each particle i in bead j is obtained by applying the chain rule of the derivative to the previous equation as

$$\begin{aligned} \mathbf{F}_i^S(\mathbf{x}^{(j)}) &= -\nabla_{\mathbf{x}_i^{(j)}} V^S(\mathbf{x}^{(j)}) \\ &= \frac{P}{P'} \sum_{j'=1}^{P'} T_{jj'} \mathbf{F}_i^S(\mathbf{x}^{(j')}). \end{aligned} \tag{2.26}$$

The total force consisting of the fast varying long range $\mathbf{F}^F$ and the slowly varying long range contribution $\mathbf{F}^S$ of the force can now use a different number of beads for each contribution. The fast varying force is not contracted and the slowly varying

one is contracted to P' beads as already described above. The total force now reads as

$$\begin{aligned} \mathbf{F}_i^{(j)} &= \frac{P}{P'} \sum_{j'=1}^{P'} T_{jj'} \mathbf{F}_i(\mathbf{x}^{(j')}) \\ &= \mathbf{F}_i^F(\mathbf{x}^{(j)}) + \frac{P}{P'} \sum_{j'=1}^{P'} T_{jj'} \mathbf{F}_i^S(\mathbf{x}^{(j')}), \end{aligned} \tag{2.27}$$

where the fast varying contribution $\mathbf{F}^F$ is evaluated in the full P-bead system and the computationally more demanding and fast varying, short range part $\mathbf{F}^S$ is evaluated on a contracted system with P' beads. The resulting computational effort is then a fraction of the one of a full P-bead calculation.

The interatomic potential of full *ab initio* structure calculations cannot be split naturally into a slowly and fast varying part because the interatomic potential is not a simple sum of multiple contributions as it was the case for the classical force fields in the original formulation of the standard ring polymer contraction scheme above. Nevertheless, a similar decomposition can be carried out in a more mathematical way and is discussed in detail in Part III.

2.3 HARTREE-FOCK SELF CONSISTENT FIELD METHOD

The rest of this chapter is devoted to the evaluation of the interatomic potential $V(\mathbf{x})$ of the MD or PIMD simulations. The simplest approximate solution to the non-relativistic the Schrödinger equation, with which this potential is obtained in electronic structure theory, can be carried out with the Hartree-Fock (HF) model [73, 74]. The full time-independent Schrödinger equation for a system with N particles and N_e electrons consists of interactions between the electrons and atomic nuclei of the system. As the nuclei are much heavier than the electrons, the Born-Oppenheimer approximation assumes that the movement of the nuclei and electrons can be fully separated [73]. This greatly simplifies the solution as the nuclear part of the Schrödinger equation is solved by the PIMD formalism and only the electronic Schrödinger equation needs to be solved here. The total wave function of the system can now be written as a product of the nuclear and electronic wave function ψ and the electronic Schrödinger equation depends parametrically on the nuclear coordinates. It consists of the kinetic energy of the electrons, the

electron-nuclear attraction, the nuclear repulsion and the electron-electron repulsion and reads in atomic units as

$$\hat{H}|\Psi\rangle = E|\Psi\rangle, \tag{2.28}$$

$$\text{where} \quad \hat{H} = \sum_{i=1}^{N_e} -\frac{1}{2}\nabla_i^2 - \sum_{i=1}^{N_e}\sum_{A=1}^{N}\frac{Z_A}{x_{iA}} + \sum_{A<B}^{N}\frac{Z_A Z_B}{X_{AB}} + \sum_{i<j}^{N_e}\frac{1}{x_{ij}}, \tag{2.29}$$

where X_{AB} denotes the distance of particle A and B, x_{iA} the distance of electron i and particle A and x_{ij} the distance between the electrons i and j. The simplest possible antisymmetric wave function that obeys the Pauli exclusion principle is a Slater determinant based on molecular orbitals that imposes an antisymmetric wave function by definition of the determinant [75]

$$|\Psi\rangle = \frac{1}{\sqrt{N_e!}}\begin{vmatrix} \psi_1(\mathbf{x}_1) & \psi_2(\mathbf{x}_1) & \cdots & \psi_{N_e}(\mathbf{x}_1) \\ \psi_1(\mathbf{x}_2) & \psi_2(\mathbf{x}_2) & \cdots & \psi_{N_e}(\mathbf{x}_2) \\ \vdots & \vdots & \ddots & \vdots \\ \psi_1(\mathbf{x}_{N_e}) & \psi_2(\mathbf{x}_{N_e}) & \cdots & \psi_{N_e}(\mathbf{x}_{N_e}) \end{vmatrix}. \tag{2.30}$$

In contrast to the previous chapter, $\mathbf{x}_i$ denotes the position of the i-th electron in this context. The molecular orbitals (MOs) $|\psi_i\rangle$ are composed of a superposition of n_{ao} atomic centered atomic orbitals $|\phi_\mu\rangle$. As the nuclei are kept constant during the solution of the electronic Schrödinger equation, this parametric dependency is omitted here and in the following for clarity. This linear superposition is often called linear combination of atomic orbitals (LCAO)

$$|\psi_i(\mathbf{x}_1)\rangle = \sum_{\mu=1}^{n_{ao}} C_{\mu,i}|\phi_\mu(\mathbf{x}_1)\rangle, \tag{2.31}$$

where the matrix $C_{\mu,i}$ are the so-called MO coefficients, i denotes one of the N_e occupied and μ a general orbital. The electronic Schrödinger equation can now be solved within this single Slater determinant approximation as a consequence of the variational theorem, where the MOs are variationally optimized to obtain ground state or the so-called Hartree-Fock energy E_{HF}

$$E_{HF} = \min_{\Psi}\langle\Psi|\hat{H}|\Psi\rangle. \tag{2.32}$$

This energy is minimized iteratively with respect to the MO coefficients until the difference between successive MO coefficients is below a predefined threshold. With this assumptions, the electrons move in the mean field created by the average charge distribution of all other electrons that names this method also as self-consistent field (SCF) method.

2.4 COUPLED CLUSTER METHODS

The missing correlation energy in the HF theory originating in the single Slater determinant ansatz is defined as difference between the exact solution of the Schrödinger equation and the HF energy. In the Coupled Cluster (CC) theory, the exact wave function that includes this correlation energy is parametrized by the exponential ansatz [39–42]

$$|\Psi_{\text{exact}}\rangle = e^{\hat{T}}|\Psi\rangle, \tag{2.33}$$

where the reference wave function $|\Psi\rangle$ is a Slater determinant of HF molecular orbitals (MOs) $|\psi_i\rangle$ from the previous section. This ansatz ensures the so-called size-extensivity, which means that the correlation energy scales linearly with the system size in the limit of an infinitely separated systems and is necessary to obtain e.g. reaction energies [74, 76, 77]. The cluster operator $\hat{T}$ is defined by

$$\hat{T} = \hat{T}_1 + \hat{T}_2 + \hat{T}_3 + \dots, \tag{2.34}$$

where the excitation operators that act on the reference wave function to generate excited wave functions read in in second quantization as

$$\hat{T}_n = \frac{1}{(n!)^2} \sum_{i,j,k,\dots} \sum_{a,b,c,\dots} t_{ijk\cdots}^{abc\cdots} \hat{c}_a^\dagger \hat{c}_b^\dagger \hat{c}_c^\dagger \cdots \hat{c}_i \hat{c}_j \hat{c}_k, \tag{2.35}$$

whereas i, j, k, ... refer as usual to occupied and a, b, c, ... to unoccupied orbitals in $|\Psi\rangle$ and $\hat{c}^\dagger$ and $\hat{c}$ are creation and annihilation operators, respectively. This inclusion of excited determinants in the ansatz for the exact wave function in Eq. 2.33 converges to the exact wave function up to a unitary transformation, when all possible excited determinants in the infinite basis set limit are included. The cluster amplitudes $t_{ijk\cdots}^{abc\cdots}$ are determined by multiple iterative equations to obtain the CC energy. A more detailed review can be found e.g. in Ref. [42].

As this energy expression is not stationary with respect to the cluster amplitudes another energy functional has been defined so that forces or any other properties which are expressed as derivatives of this wave function can be calculated. This energy functional reads as [78–81]

$$\tilde{E} = \langle \Psi | (1 + \hat{\Lambda}) e^{-\hat{T}} \hat{H} e^{\hat{T}} | \Psi \rangle \tag{2.36}$$

where the de-excitation operator $\hat{\Lambda}$ has a similar structure like the $\hat{T}$ operator

$$\hat{\Lambda} = \hat{\Lambda}_1 + \hat{\Lambda}_2 + \hat{\Lambda}_3 + \dots, \tag{2.37}$$

and the de-excitation operators read in second quantization as

$$\hat{\Lambda}_n = \frac{1}{(n!)^2} \sum_{i,j,k,\dots} \sum_{a,b,c,\dots} \lambda_{abc\dots}^{ijk\dots} \hat{c}_i^\dagger \hat{c}_j^\dagger \hat{c}_k^\dagger \cdots \hat{c}_a \hat{c}_b \hat{c}_c. \tag{2.38}$$

The energy functional in Eq. 2.36 is stationary with respect to the λ amplitudes for a given solution to the cluster amplitudes, which is a necessary condition to formulate energy derivatives.

In this notation, the coupled cluster singles and doubles (CCSD) method truncates $\hat{T}$ in Eq. 2.34 and $\hat{\Lambda}$ in Eq. 2.37 after the two-body cluster and λ contributions. The coupled cluster singles and doubles with non-iterative triples CCSD(T) method is an extension of CCSD, that approximates second order triples amplitudes $\hat{T}_3^2$ with perturbation theory from the $\hat{T}_2$ amplitudes and adds higher order corrections to the CCSD energy [82–84]. Both methods are used in the following CC-MD and CC-PIMD simulations.

Part II

ACCELERATION OF QUANTUM MOLECULAR DYNAMICS SIMULATIONS

3

"ON-THE-FLY" COUPLED CLUSTER PATH INTEGRAL MOLECULAR DYNAMICS

In the previous chapter, the fundamental ideas of path integral molecular dynamics (PIMD) and coupled cluster (CC) have been introduced. The latter is already the golden standard in single point calculations and in the following it is combined with PIMD, which includes nuclear quantum effects (NQE) at finite temperature in a systematic way. This combination of the CC-based PIMD will be christened as *quantum molecular dynamics* and is to our knowledge the first MD and PIMD simulation at this highly accurate level of theory. The high computational cost associated with such a simulation can be reduced by exploiting the fact that subsequent CC calculations are very similar as the nuclear positions changed only slightly. Initially, the molecular orbitals that are used for the calculation of the HF reference wave function are extrapolated in a similar fashion than the second generation Car-Parrinello approach of Kühne *et al.* [43, 44] as a starting point to reduce the computational cost. The extension of this method to also propagate the cluster and $\hat{\Lambda}$ amplitudes in CC theory, whose solution consumes the major part of the electronic structure calculations, will be presented in the next chapter.

This approach is used to investigate investigate the impact of nuclear quantum effects on the structure and the nuclear magnetic shielding tensor of the protonated water dimer as shown in Fig. 3.1. This system has been extensively studied using conventional semi-classical ab-initio MD at the second order Møller-Plesset perturbation theory MP2 level of theory [86, 87] and with DFT-based PIMD [12] and is therefore a good candidate as initial benchmark calculation.

Parts of these results have already been published in Ref. [37] and are reproduced here with some modifications.

(a) classical simulation (CC-MD) (b) quantum simulation (CC-PIMD)

Figure 3.1: Representative snapshots of the protonated water dimer with the CC-MD and CC-PIMD simulations. The bonds of the centroid of the system are only drawn to guide the eye for easy comparison.

3.1 EXTRAPOLATION OF MOLECULAR ORBITALS

In second generation Car-Parrinello, a coupled electron-ion dynamics is designed so that the electronic degrees of freedom are very close to the instantaneous electronic ground state. This is achieved by adopting the always stable predictor and corrector integrator of Kolafa to the propagation of the molecular orbitals (MOs) and density operator [43, 88]. As the dynamics of the single-particle density operator $\hat{\rho} = \sum_i |\psi_i\rangle\langle\psi_i|$ is much smoother than the one of the MOs, the former can be much more easy predicted. Therefore, the predicted density operator $\hat{\rho}^p(t)$ at time t is estimated by the K previous $\hat{\rho}(t - m\Delta t)$ ones at times $t - m\Delta t$ where $m \in \{1, \ldots, K\}$ and is then used as projector on the occupied subspace of the most recent MOs at time $t - \Delta t$. The predicted MOs can then be obtained with

$$|\psi_i^p(t)\rangle \approx \underbrace{\sum_{m=1}^{K} (-1)^{m+1} m \frac{\binom{2K}{K-m}}{\binom{2K-2}{K-1}} \hat{\rho}(t - m\Delta t)}_{\hat{\rho}^p(t)} |\psi_i(t - \Delta t)\rangle, \tag{3.1}$$

which is accurate and time reversible up to $\mathcal{O}(\Delta t^{2K-2})$ and K is also-called predictor length [89]. In contrast to the original second generation Car-Parrinello approach, where a single preconditioned electronic gradient is applied to the resulting MOs as the corrector, the MOs are here only used as initial guess for the Hartree-Fock

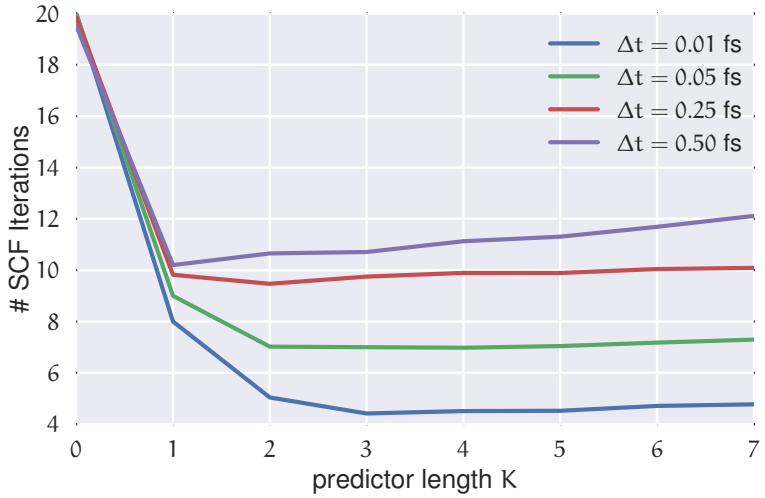

Figure 3.2: Efficiency of the MO extrapolation for the example of the protonated water dimer with a cc-pVDZ basis [91] measured by the average number of SCF iterations of 50 consecutive MD steps needed to converge to the ground state energy as function of different time steps Δt and different predictor length or number of most recent density operators K. The smaller the time step the less number of iterations are needed to converge to the ground state.

self-consistent field cycle [90] and then fully converged to the ground state, see also Sec. 2.3.

The efficiency of this approach is found to depend on the time step employed in the MD simulation. The smaller the time step the closer are the predicted MOs to the fully converged electronic ground state. This can be seen in the average number of iterations needed to converge to the true ground state in Fig. 3.2, where for smaller time steps an up to five-fold speed-up has been observed, although so far only in the HF part. Since the total calculation is dominated by solving the cluster and $\hat{\Lambda}$ amplitudes, the overall speed-up is just a few percent. A more detailed breakdown of the distribution of the time in the total calculation will be presented in the next chapter (E.g. see Fig. 4.3 for another atomic combination in the gas phase. For more details, see that chapter.), where also the amplitudes are extrapolated. In the next section however, the results for the first *quantum molecular dynamics* simulation at the CC level of theory are presented for the case of the protonated water dimer and MO extrapolation is employed throughout.

3.2 NUCLEAR QUANTUM EFFECTS OF PROTONATED WATER DIMER

The following CC-MD and CC-PIMD simulations were conducted using a modified version of i-PI [92], whereas the forces were calculated at the CCSD/cc-pVDZ level of theory [91, 93–96] using the CFOUR program package [97, 98]. They were all performed in the canonical NVT ensemble at 300 K using a discretized time step of 0.25 fs for 28 ps. The nuclear Schrödinger equation is found to be essentially exactly solved for $P = 32$ beads that is hence employed throughout. For the purpose of quantifying the impact of NQE, an additional CC-MD simulation with classical nuclei ($P = 1$) has been performed, which altogether amounts to nearly 4 million CCSD/cc-pVDZ calculations. The isotropic nuclear shielding with and without NQE has been calculated as an ensemble average over 4000 decorrelated snapshots at the CCSD(T)/cc-pVTZ level of theory [99, 100].

Comparing the results of the CC-MD and CC-PIMD simulations, the inclusion of NQE is found to just leads to a slightly more delocalized quantum proton and entails only a tiny increase of the average intermolecular O-O bond length from 2.417 Å to 2.424 Å. Even though the qualitative trend is identical to previous DFT-based AI-PIMD simulations, the latter yields average bond lengths that are longer by about 0.03 Å [12]. Nevertheless, the importance of NQE is much more apparent whenever light atoms such as hydrogen are involved as demonstrated by the dramatic change of the $O_1H^+O_2$ angle that decreases from 168.99° to 164.29°, which is due to the substantially enhanced anharmonicity of the bending angle. In any case, the difference of the eventual bending angle by $9° - 11°$ from DFT-based AI-PIMD and more accurate, but static CC calculations [12, 101–103], respectively, is a striking manifestation of the importance to sample both thermal and quantum fluctuations of many coupled degrees of freedom concurrently.

The rest of this section will focus on the nature of the shared quantum proton. On the one hand static calculations at the HF level of theory predict an asymmetric bonding where the proton is covalently bonded to either one of the water molecules ($H_2O\text{-}H^+ \cdots OH_2$), which suggest that the proton moves within a double-well potential. On the other hand, however, accurate MP2 and CC calculations predict that the proton is shared between the water molecules ($H_2O \cdot \cdot H^+ \cdots OH_2$) [101, 102, 104, 105], i.e. a single-well potential.

As can be seen in Fig. 3.3, the free-energy distributions of both of our simulations obey a single-well only, although the one of the CC-PIMD calculation is much more

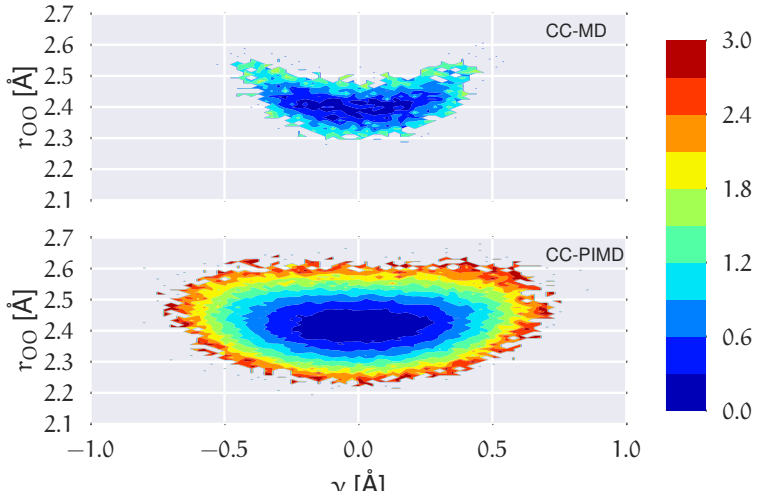

Figure 3.3: Free energy distribution in kcal/mol of the shared proton of our CC-MD and CC-PIMD simulations as a function of the intermolecular O-O distance and the proton reaction coordinate $\nu = r_{O_1H^+} - r_{O_2H^+}$. Reproduced from Ref. [37] with permission from the PCCP Owner Societies.

delocalized. The latter is to be expected and is in qualitative very good agreement with previous AI-PIMD simulations at the DFT level [12, 16].

Moreover, the inclusion of NQE reduces the correlation between the proton reaction coordinate $\nu = r_{O_1H^+} - r_{O_2H^+}$ of Tuckerman *et al.* [12] and the intermolecular O-O distance, which is in overall excellent agreement with the work of Limbach *et al.* [106]. For the purpose of studying the delocalization in more detail, the O-H pair correlation function (PCF) is decomposed into two separate contributions from the covalently bound intramolecular O-H bond and the hydrogen-bonded O··H$^+$ as shown in Fig. 3.4. From this it follows, that the proton experiences rather large quantum fluctuations, which results in unexpectedly large excursions between the water molecules. In fact, the two distributions are found to exhibit a sizable overlap in the CC-PIMD simulation, which corresponds to the fact that due to NQE the proton is occasionally allowed to approach the O atom even closer than its respective covalently-bonded H atom. By contrast, in the semi-classical CC-MD simulation, the associated overlap is very small, with the result that the proton is essentially never closer to one of the O atoms than the typical covalent O-H bond length. In other words, even though the probability of these transient excursions is rather small, they are emerging much more often than generally appreciated. Moreover,

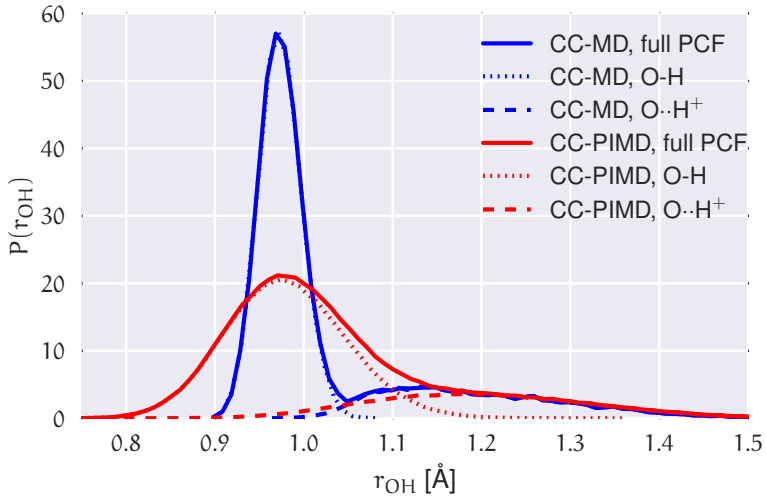

Figure 3.4: Total O-H PCF as obtained by CC-MD and CC-PIMD simulations and its decomposition into covalent (O-H), as well as hydrogen-bonded (O · ·H^+) contributions. Reproduced from Ref. [37] with permission from the PCCP Owner Societies.

the effect of these quantum fluctuations is significant and is not seen in simulations with classical nuclei. In that respect the present effect is similar to the recently observed transient proteolysis events in liquid water [26].

Nuclear magnetic shielding is one of the most sensitive probes for detecting small changes in molecular electronic structure. It is commonly used to assess the accuracy of theoretical electronic structure methods, and has recently been employed to study the quantum nature of the proton in hydrogen-bonded systems [108]. In order to investigate the impact of NQE on the electronic structure, in Fig. 3.5 the ^{1}H isotropic nuclear magnetic shielding σ is shown as a function of the proton reaction coordinate ν. The shielding tensor of the proton is found to strongly depend on ν, which immediately suggests that the same may also hold for the recently found asymmetry in liquid water [32–34]. Although the correlation is somewhat more pronounced than in the previous static calculations of Limbach *et al.* [106], the agreement is generally very good. Including NQE, the average isotropic nuclear shielding increases by 0.23 ppm, which is a direct consequence of the aforementioned transient excursions of the proton [26]. In fact, all the principal components of the shielding tensor show small, but significant differences between the simulations with classical and quantum nuclei. Furthermore, using classical nuclei the

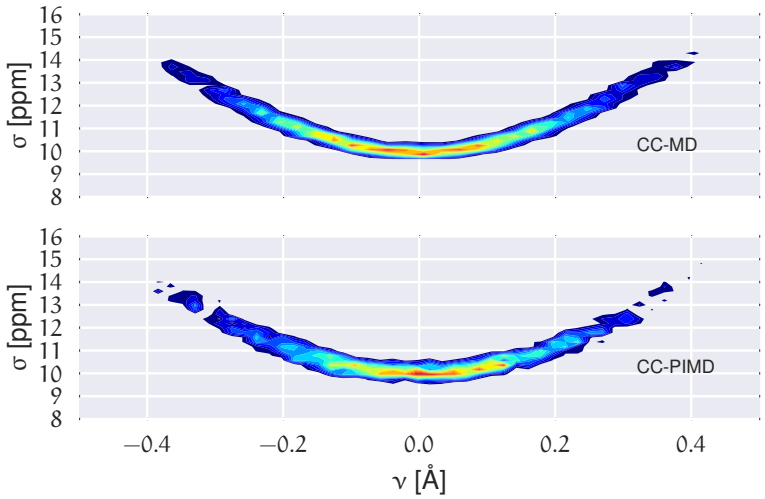

Figure 3.5: Distribution of the isotropic nuclear magnetic shielding of the proton σ in units of ppm as a function of the proton reaction coordinate ν. Reproduced from Ref. [107] with permission from the PCCP Owner Societies.

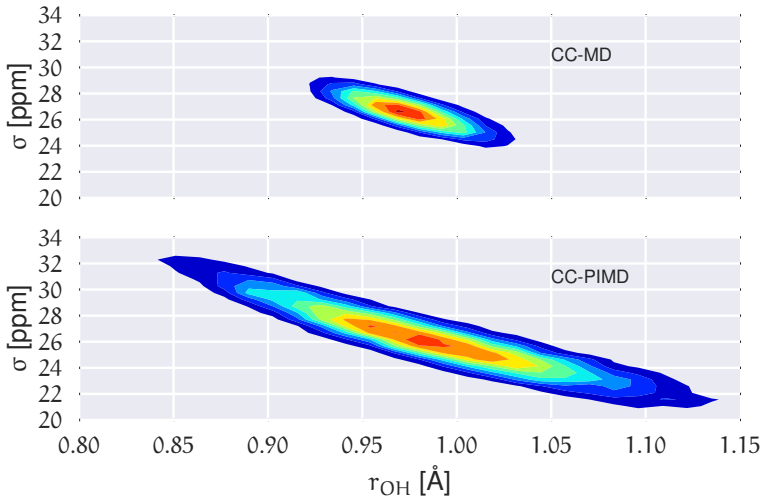

Figure 3.6: Distribution of the isotropic nuclear magnetic shielding of the four hydrogens σ in units of ppm as a function of the hydrogen–oxygen distance r_{OH}. Reproduced from Ref. [107] with permission from the PCCP Owner Societies.

differences in the isotropic nuclear shielding of the proton between HF and CC is 0.64 ppm, while including nuclear NQE reduces the difference to −0.31 ppm only. The fact that for this quantity the CC and NQE corrections are competing immediately suggests that the level of theory used for describing the electronic structure is less important in PIMD calculations than in MD. To study the impact of NQE on the vapor-to-liquid chemical shift, the hydrogen-bonded proton is considered here as the liquid-like proton to mimic the situation of an excess proton solvated in water and the remaining hydrogen atoms are considered as gas-like. The isotropic nuclear magnetic shielding values of the latter as a function of the hydrogen–oxygen distance r_{OH} are shown in Fig. 3.6. Even though, at the presence of NQE, the shielding is much more delocalized, the mean value differ by less than one ppm, at variance to the proton of Fig. 3.5. As a consequence, the NQE induced change of our vapor-to-liquid shift estimate is −0.67 ppm, which again is mainly a result of the transient proton excursions and as such another manifestation on the importance of NQE [26]. The corresponding value at the HF level of theory is 0.25 ppm, which means that the NQE and CC corrections are cooperative, but again the former slightly more important. Fig. 3.7 for instance reveals a clearly different spatial dependence for the maximum eigenvalue of σ. Furthermore, the difference between the largest and smallest eigenvalues of the shielding tensor (the span) decreases by 1.7 ppm in case of the CC-PIMD simulation including NQE. These components of the shielding tensor can be readily probed by solid state NMR [109–111] and via the NMR relaxation even in the liquid state [112]. This way would possibly provide an experimental way to measure the geometry and the strength of a hydrogen bond which is more sensitive than the widely used isotropic shielding. It should be noted that we expect NQE to be even more pronounced if the solvation environment of the proton were less symmetric. This is investigated in detail in the next chapter.

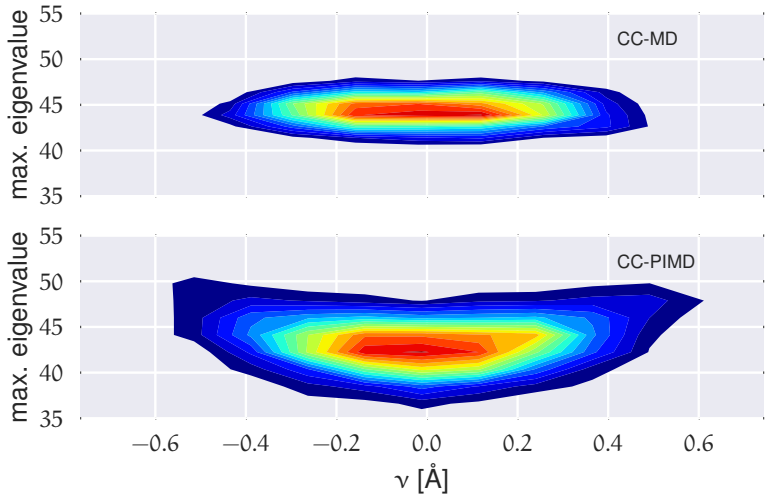

Figure 3.7: Distribution of the maximum eigenvalue of the proton magnetic shielding tensor in units of ppm with respect to the proton reaction coordinate ν. Reproduced from Ref. [107] with permission from the PCCP Owner Societies.

3.3 CONCLUSIONS

In this chapter, it has been shown that the extrapolation scheme from the second generation Car-Parrinello approach can be directly applied to Hartree-Fock. This is of no surprise as the equations of Kohn-Sham Density Functional Theory are similar to the one from Hartree-Fock in Sec. 2.3. Furthermore, the CC-based PIMD simulation has been able to systematically quantify properties of small molecules in an highly accurate fashion. Finally, we would like to note in passing that this is to the best of our knowledge first MD simulation at the CC level of theory and the first CC-based *ab initio*-PIMD simulation ever realized.

4

ACCELERATED "ON-THE-FLY" COUPLED CLUSTER PATH INTEGRAL MOLECULAR DYNAMICS

The computational cost of the electronic structure calculations within the MD simulation can be substantially reduced by finding a good initial guess to the iterative equations in the HF and CC theory. Exploiting the knowledge of the MOs and amplitudes of the previous calculations, this initial guess can be efficiently calculated and the electronic degrees of freedom are kept very close to the Born-Oppenheimer surface by design. In the previous chapter (see also Ref. [37]), it was shown that the MOs can be propagated with the predictor-corrector integrator of Kolafa [43, 88] so that the self-consistent field (SCF) equations in HF theory converge considerably faster to the ground state. In this chapter, the cluster and $\hat{\Lambda}$ amplitudes in the CC theory are transformed and extrapolated in an efficient way to reduce the computational cost of the dominating solution of the iterative amplitude equations.

This approach is applied to a system consisting of a proton bound between a water and a formaldehyde molecule as shown in Fig. 4.1. As we expected a more severe changes to the properties of this system due to the correct treatment of the additional quantum degrees of freedom in the asymmetric environment of the proton, the results of this simulation can directly be compared to the symmetric proton system from the previous Chapter 3. To investigate the structural differences introduced by tunneling and zero-point energy at room temperature, the nuclear magnetic shielding tensor of this system is discussed in detail.

(a) classical simulation (CC-MD) (b) quantum simulation (CC-PIMD)

Figure 4.1: Representative snapshots of the asymmetric proton system consisting of a water, a formaldehyde and a proton with the CC-MD and CC-PIMD simulations. The bonds of the centroid of the system are only drawn to guide the eye for easy comparison.

4.1 EXTRAPOLATION OF CLUSTER AND $\hat{\Lambda}$ AMPLITUDES

The biggest fraction of the computational cost of a force calculation is caused by the solution of the cluster and $\hat{\Lambda}$ amplitudes. This part of the calculation can be reduced by providing a good initial guess as a starting point for solving the cluster and $\hat{\Lambda}$ equations. As the solution of the cluster and $\hat{\Lambda}$ amplitudes depend (implicitly) on the MOs as a basis for calculating the correlation energy, they inherit also some properties of the MOs, which are important to note in order to invent a new, computationally less demanding extrapolation scheme. The HF energy expression in Eq. 2.32 is invariant to unitary transformations of the orbitals. This implies that many MOs result in the same HF energy and are equivalent in this respect. This non-uniqueness introduces spurious changes in the amplitudes over the course of the simulation which need to be separated out from physical changes of the changing geometry over time. The former change can be substantially reduced by transforming the amplitudes to an intermediate representation, that is approximately constant over time. This can be achieved by transforming the amplitudes to the full orthogonal basis set with the help of the symmetrically orthogonalized MO coefficients $\tilde{C}_{\mu,\nu} = \sum_{\gamma}^{n_{ao}} \langle \phi_\mu | \phi_\gamma \rangle^{1/2} C_{\gamma,\nu}$ from Eq. 2.31. As the cluster and the $\hat{\Lambda}$ amplitudes have a similar structure, both transformations can be carried out in analogy. For the sake of simplicity the transformations for the one-body amplitudes

are shown in the further outline of this work and higher-order amplitudes are transformed for each added body contribution in equivalence. For the one-body cluster contribution from the previous time step $t - \Delta t$ (denoted as the superscript $^{t-\Delta t}$ in the following) the transformation to the full orthogonal basis reads as

$$\tilde{t}_{\mu}^{\nu,t-\Delta t} = \tilde{C}_{\mu,i}^{t-\Delta t} t_{i}^{a,t-\Delta t} \tilde{C}_{\nu,a}^{t-\Delta t^{\top}}. \tag{4.1}$$

The back-transformation of this intermediate representation in the orthogonal basis onto the new basis set of the changed geometry at time t reads as

$$t_{i}^{a,t} = \tilde{C}_{\mu,i}^{t^{\top}} \tilde{t}_{\mu}^{\nu,t-\Delta t} \tilde{C}_{\nu,a}^{t}. \tag{4.2}$$

The net transformation of these two equations boils down to the first order change of basis with the bypass over the orthogonal basis as an intermediate representation. This would only be exact if the amplitudes stayed constant over time as no extrapolation in time has been carried out so far. As this is not the case, the change of the amplitudes over time must be explicitly taken into account by the extrapolation of the previous cluster amplitudes as in Eq. 4.1. In the full orthogonal basis set, the physical change of the amplitudes $\tilde{t}_{ijk\cdots}^{abc\cdots}$ can be extrapolated to the next time step t based on the most recent K amplitudes with the always stable predictor by Kolafa [88] with

$$\tilde{t}_{\mu}^{\nu,t} \approx \sum_{m=1}^{K} (-1)^{m+1} m \frac{\binom{2K}{K-m}}{\binom{2K-2}{K-1}} \tilde{t}_{\mu}^{\nu,t-m\Delta t}, \tag{4.3}$$

where K denotes the predictor length (see also Ref. [37] and Sec. 3.1).

For the higher-order-body operators, similar transformations for each additional occupied and unoccupied index needs to be carried out. The formal scaling of the CC theory is not affected by this transformations as only standard matrix multiplications are involved.

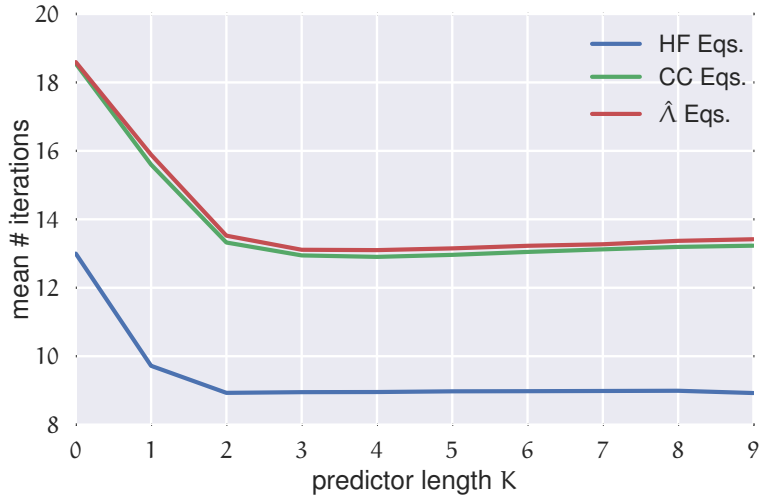

Figure 4.2: Mean number of iterations needed to fully converge the cluster and $\hat{\Lambda}$ equations as a function of the predictor length or number of most recent items K in the extrapolation.

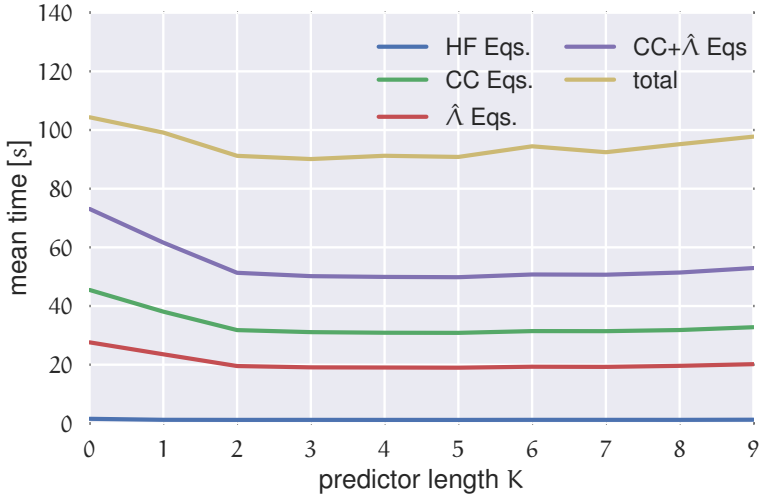

Figure 4.3: Detailed timing distribution of a CCSD force calculation in time to solution of the HF equations, cluster and $\hat{\Lambda}$ amplitudes as a function of the predictor length or number of most recent items K in the extrapolation.

The efficiency of this approach is such that even with employing the conventional convergence accelerator used in many electronic structure programs (direct inversion in the iterative subspace, DIIS [113, 114]) to the amplitudes, about 30% less iterations of the cluster and the $\hat{\Lambda}$ amplitudes are needed to fully converge to the electronic ground state, see Fig. 4.2[1]. The distribution of the total run time is depicted in Fig. 4.3. The fraction of the run time to solve the cluster and $\hat{\Lambda}$ amplitudes is about 70.0% in this case with the standard algorithm of starting from second order Møller-Plesset perturbation theory (MP2) amplitudes as initial guess. With extrapolation, this fraction diminishes to 53.7%. The biggest time savings comes from the cluster amplitudes which take a fraction of 43.5% without and 33.3% with extrapolation. The corresponding values of the $\hat{\Lambda}$ amplitudes are 26.5% and 20.4% respectively. The HF part is also running faster as can be seen in the reduction of needed number of iterations in Fig. 4.2. Yet, as it only contributes a tiny fraction to the overall time to calculate the gradient (see Fig. 4.3), this speed-up is not noticeable in practice. The total impact on the running time of one force calculation is that this approach takes about 13.6% less time than the standard algorithm.

4.2 APPROXIMATION WITH INCOMPLETELY CONVERGED CC AMPLITUDES

So far the cluster and $\hat{\Lambda}$ amplitudes have been fully converged to the electronic ground state by iterating through the iterative equations until the change of the amplitudes is below a predefined threshold. As already shown in the section before, the cluster amplitudes take a bigger fraction of the total run time, so an additional approximation of them will greatly impact the running time. By iterating the cluster amplitudes only twice through these equations, the cluster amplitudes are now incompletely converged and as CC is not a variational theory this approximate solution can be below or above the true energy value. To verify this expected behavior, a short MD simulation has been done with only two iterations of the cluster amplitudes. This trajectory is then retraced by a fully converged solution of the cluster and $\hat{\Lambda}$ equations to compare the resulting energy and forces with the true electronic ground state. In Fig. 4.4, the difference of the energy and the forces between the approximate and fully converged solution is shown. The energy deviation is always below 10^{-5} Hartree with an average of $1.13 \cdot 10^{-6}$ Hartree. The

1 Without DIIS as convergence accelerator, the number of iterations are reduced by a bigger fraction of about $35 - 40\%$. Yet, as the mean number of iterations are about doubled (and so does the time to solution of the cluster and $\hat{\Lambda}$ amplitudes) DIIS will be employed throughout.

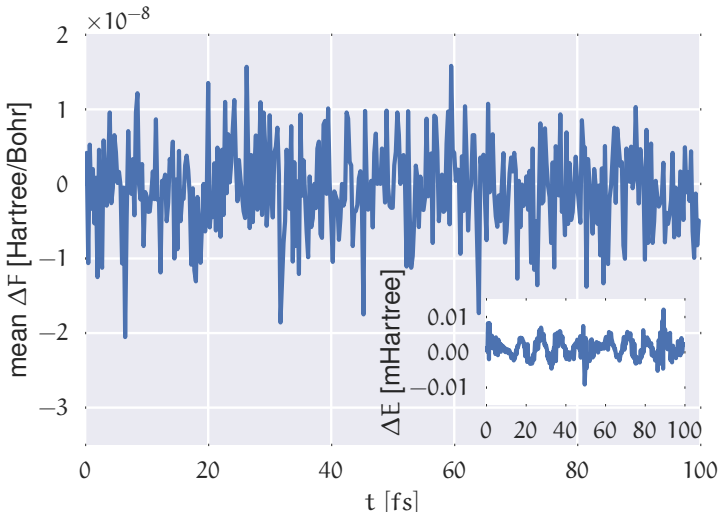

Figure 4.4: Energy and force deviation over time of a MD simulation with two iterations of the cluster equations and fully converged $\hat{\Lambda}$ equations.

mean force deviation is even smaller with $-7.16 \cdot 10^{-10}$ $\frac{\text{Hartree}}{\text{Å}}$ averaged over the whole simulation and at maximum $1.58 \cdot 10^{-8}$ $\frac{\text{Hartree}}{\text{Å}}$. This means that on average the error is even smaller than introduced with the approximation of taking less iterations and it is advantageous that CC is non-variational. This new approach hugely impacts the total running time as can be seen when comparing the original timing distribution in Fig. 4.3 with the timing distribution with two iterations in Fig. 4.5. The fraction of solving the cluster and $\hat{\Lambda}$ equations shrinks from 70.0% to now only 36.2%. The cluster equations take now with less iterations the fraction of 7.8% where they needed 43.6% of the running time before. The time of solving the cluster amplitudes is reduced by 88.2% and the total running time is reduced by 38.8% with this approach while the resulting MD simulation is very similar to the fully converged one.

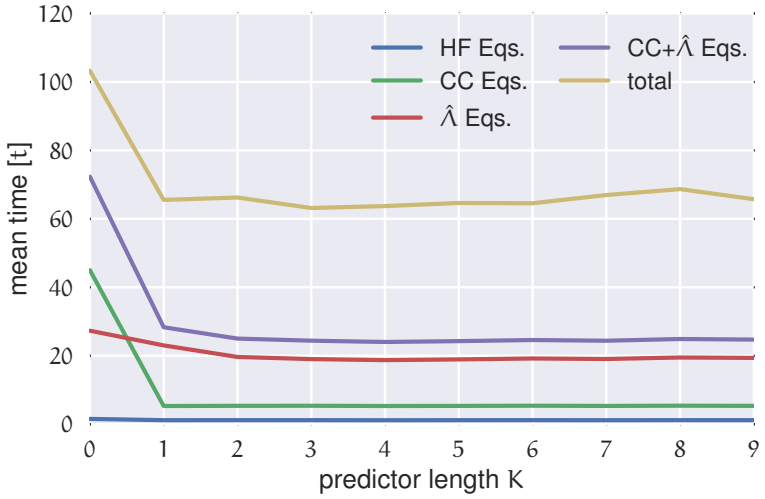

Figure 4.5: Detailed timing distribution of a CCSD force calculation with two iterations of the cluster amplitudes in time to solution of the HF equations, cluster and $\hat{\Lambda}$ amplitudes.

4.3 NUCLEAR QUANTUM EFFECTS OF AN ASYMMETRIC PROTON

The following CC-MD and CC-PIMD simulations were conducted using i-PI [92], whereas the forces were calculated at the CCSD/cc-pVDZ level of theory [91, 93–96] using a modified version PSI4 program package [115, 116] with included amplitude transformation functionality. They were all performed in the canonical NVT ensemble at 300 K using a discretized time step of 0.25 fs for 5.5 ps with $P = 32$. For the purpose of quantifying the impact of NQE, an additional CC-MD simulation with classical nuclei ($P = 1$) has been performed. The isotropic nuclear shielding with and without NQE has been calculated as an ensemble average over each time 1000 decorrelated snapshots at the CCSD(T)/cc-pVTZ level of theory [99, 100] with the CFOUR program package [97, 98].

The inclusion of NQE in the CC-PIMD simulations lead to a broadening of the covalently bound hydrogens either to the oxygen or carbon, for instance see the C–H pair correlation function (PCF) in Fig. 4.6, where the first peak is cut by a bit less than one third. This broadening of covalently bound hydrogens can be seen commonly and is in line with the result of the protonated water dimer from the previous chapter. The average distances between most atoms increase slightly in the subpercentage range. One exception is the oxygen oxygen distance, that decreases

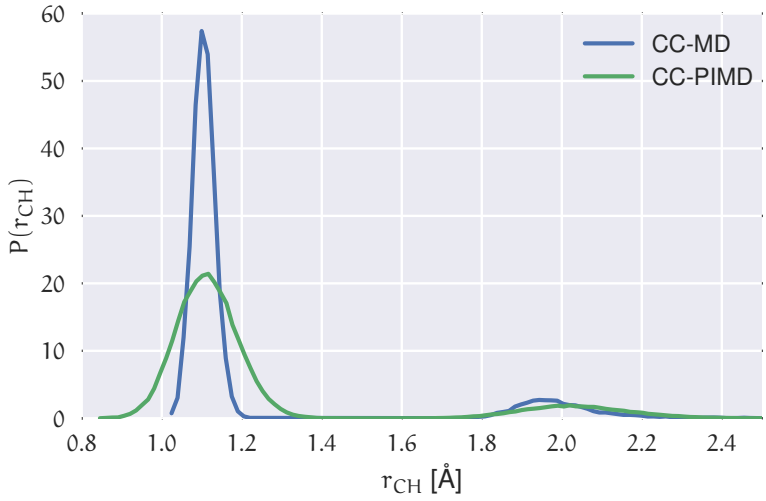

Figure 4.6: Total C–H PCF obtained with CC-MD and CC-PIMD simulations that shows the intramolecular C–H bond and the distribution of the carbon proton distance C–H^+.

slightly from 2.445 Å to 2.443 Å which shows an opposite trend to the results of the protonated water dimer. Nevertheless this change is well below the standard deviation and the distribution of the O–O distance does not differ significantly. The most dramatic changes occur in the O–C double bond in Fig. 4.7 and the $O_1H^+O_2$ angle in Fig. 4.8. The $O_1H^+O_2$ bending angle of the proton decreases when employing NQE as dramatically as in the previous chapter for the case of the protonated water dimer from 168.2° to 164.9°. The O–C distribution is much more delocalized, whereas the mean is almost the same as it increases only by 0.001 Å. This once more highlights the importance of sampling the additional quantum fluctuations.

As indicated in the free energy distribution of the proton reaction coordinate defined in analogy to the previous chapter [12, 37] as difference of the distances from the proton to both oxygens $\nu = r_{O_{H_2O}H^+} - r_{O_{CH_2O}H^+}$ in Fig. 4.9, the proton is located closer to the formaldehyde than to the water molecule in the classical CC-MD simulation. In the quantum simulation, the proton is fully delocalized between both molecules, the bias to favor the formaldehyde is reduced greatly but still visible. The average position is moved from $\nu = 0.206$ Å to $\nu = 0.135$ Å and the fraction to be located near the formaldehyde is reduced from 81.7% to 61.1%. These large excursions of the proton can be seen already in the total O–H PCF in Fig. 4.10 and can be made even more visible with the decomposition of the total

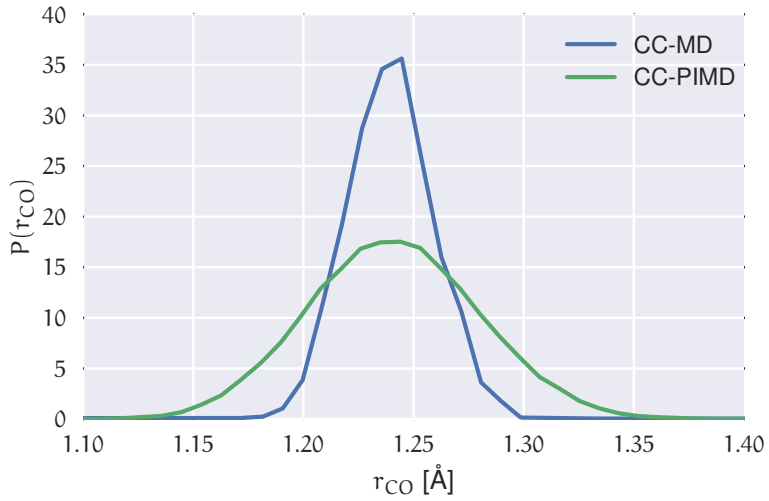

Figure 4.7: Total O–C PCF obained with CC-MD and CC-PIMD simulations that shows the NQE enhanced broadening of the distribution of the O–C double bond.

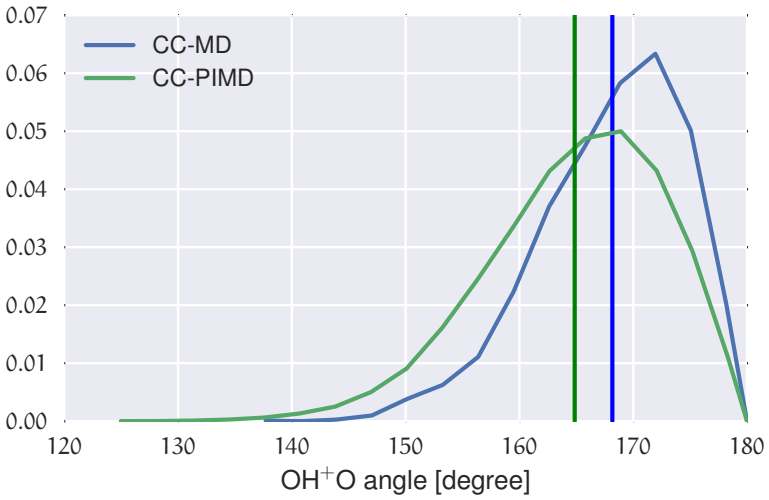

Figure 4.8: Distribution of the $O_1H^+O_2$ bending angle of the CC-MD and CC-PIMD simulations that shows the anharmonicity of the shared proton distribution. The vertical lines denote the mean values of the bending angle in the classical and quantum simulation.

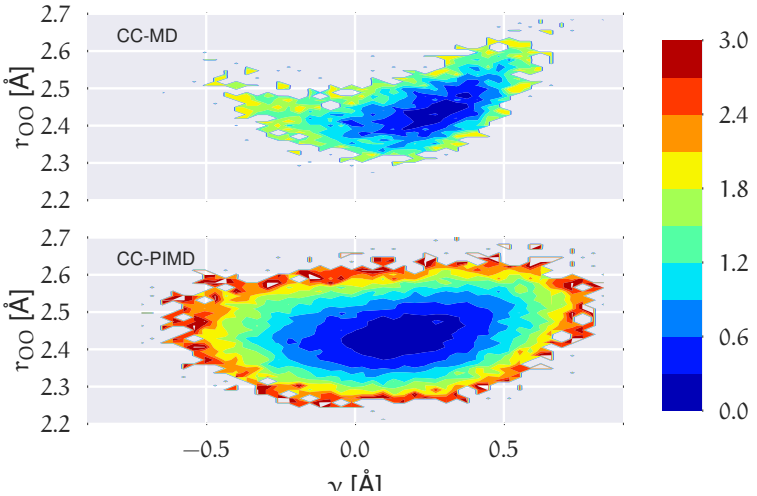

Figure 4.9: Free energy distribution in kcal/mol of the shared proton in the CC-MD and CC-PIMD simulations as a function of the intermolecular O–C distance and the proton reaction coordinate ν.

O–H^+ PCF of the proton and the two oxygens of the formaldehyde and the water in Fig. 4.11. Whereas in the classical simulation the proton is bound stronger to the formaldehyde and is distributed in an asymmetric fashion from the water, the O_{H_2O}–H^+ distribution becomes more harmonic in the quantum simulation. The total PCF transforms from two distinct peaks to one common peak, which makes it indistinguishable whether it is composed of one underlying contribution or two and emphasizes the importance of sampling the additional quantum degrees of freedom in addition to thermal fluctuations.

The very high sensitivity of the NMR shielding tensor (σ) to the slightest perturbations in electronic structure and nuclear configuration makes it a stringent test of *ab initio* methods, a bond stretching as small as 0.0001 Å can induce a chemical shift difference of 0.1 ppm [118]. In general, the effect of nuclear motion on the NMR shielding tensor is known to be important. Classical rovibrational averaging on the Born-Oppenheimer surface has demonstrated that nuclear fluctuation effects can be as large as the effects of including post-HF electron correlation on σ [26, 119, 120]. Beyond classical nuclear vibrations, PIMD has been employed more recently to investigate the influence of nuclear quantum fluctuations on the nuclear shielding tensor [22, 26, 121, 122]. The few results available indicate that for quantitative agreement with experiment, a proper accounting for NQEs is required.

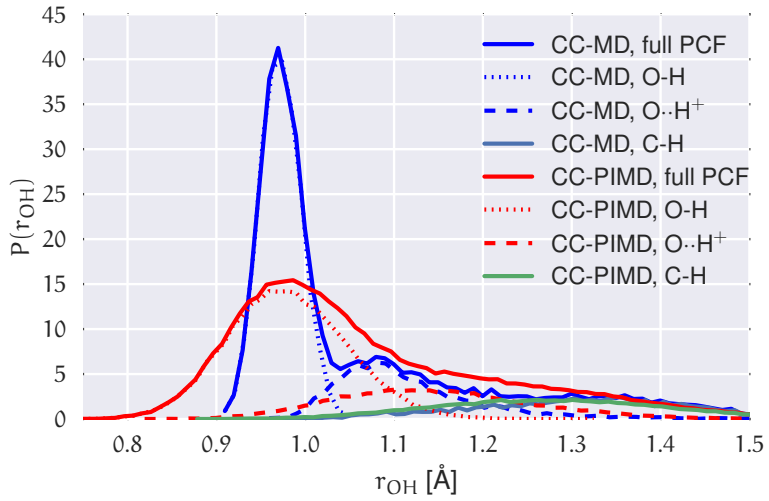

Figure 4.10: Total O–H PCF obtained with CC-MD and CC-PIMD simulations and their decomposition into covalent (O–H), hydrogen-bonded ($O \cdot\cdot H^+$) and the oxygen–hydrogen contribution from the covalent bound hydrogen to the carbon atom (C–H).

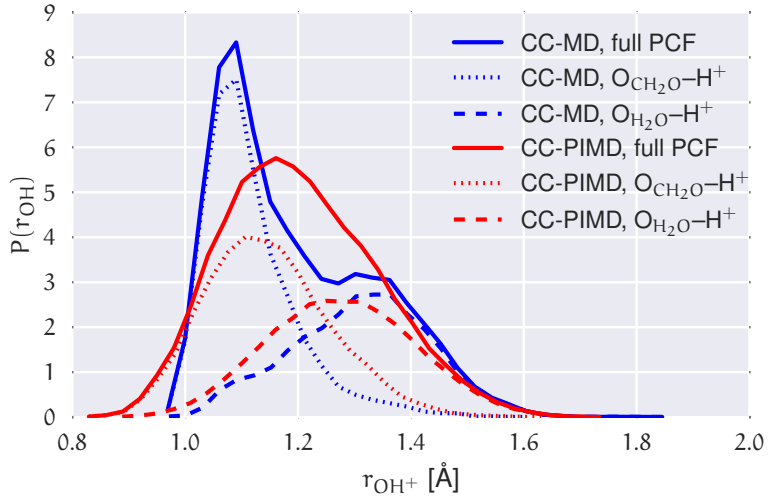

Figure 4.11: Total $O–H^+$ PCF obtained with CC-MD and CC-PIMD simulations and their decomposition into the contributions of the formaldehyde's oxygen (O_{CH_2O}) and the water's oxygen (O_{H_2O}) to the proton (H^+).

Including NQEs has been found, for instance, to alleviate the need for linear regression to improve the agreement between theoretical and experimental shielding values [123], suggesting that this long-standing issue could be due to the neglect of nuclear quantum fluctuations. PIMD-based estimates of the ^{1}H-^{2}D secondary isotope effects on the ^{13}C shieldings in alanine have also been found to be in excellent agreement with experiment, whereas MD failed to reproduce the experimental data. In general however, the quantitative contribution of nuclear quantum fluctuations to the ensemble-averaged shielding tensor, that is on top of the classical vibrational motion, is not generally known. Moreover, one generally needs to investigate the influence on different tensor components, as the effect on specific tensor components can substantially differ from the average effect on the isotropic shielding value. In the following, the nuclear magnetic shielding tensor is calculated as an ensemble average over 1000 snapshots of either the CC-MD or the CC-PIMD trajectory. Compared to static *ab initio* calculations that incorporate rovibrational averaging, a PIMD-based approach requires neither a perturbation treatment nor a truncated Taylor expansion, as it incorporates zero point, anharmonicity and tunneling effects in the systematic sampling of the respective snapshots from the ensemble. Furthermore, all correlation effects are treated consistently in the NMR calculations based on the CC level of theory [98–100]. By comparing the ensemble-averaged shielding tensors from the CC-MD and CC-PIMD trajectories, together with the Hartree-Fock counterparts, one can systematically and quantitatively assess the influence of electron correlation, classical nuclear fluctuations, and genuine nuclear quantum fluctuations, on the components of the NMR shielding tensor.

In Fig. 4.12, the ^{1}H isotropic nuclear magnetic shielding σ is shown as a function of the proton reaction coordinate ν. Compared to the CC-MD, the CC-PIMD proton is more shared between both molecules and less strongly attached to the formaldehyde. This agrees with previous findings [26, 123] and reflects the shift of the distribution of the proton as it lingers more in a shared configuration. The distribution of σ in PIMD as a function of the reaction coordinate shows the typical distribution one expects from a proton "trapped" between two cites. Although such a non-linear distribution (as contrasted to the ellipsoidal one in MD) could lead to shift in σ [108], in our case it does not, as the increase in σ induced by more sampling of configurations where the proton is shielded is counteracted by a shift in the equilibrium reaction coordinate towards the middle.

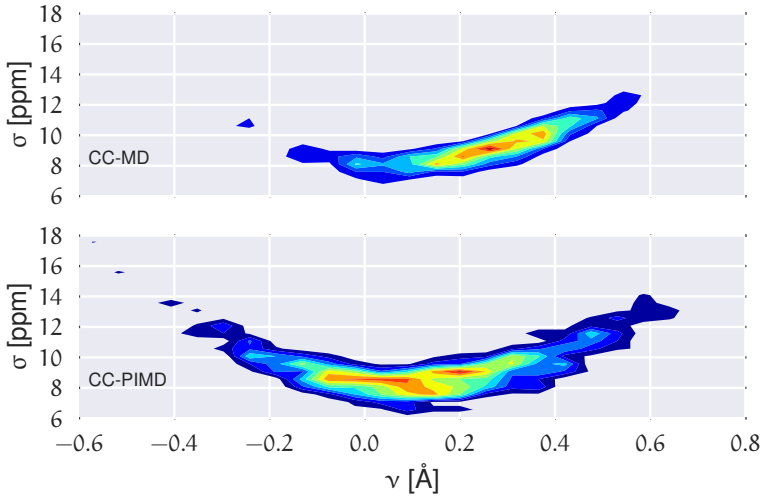

Figure 4.12: Distribution of the isotropic nuclear magnetic shielding σ of the proton bound between the water and formaldehyde in units of ppm as a function of the proton reaction coordinate ν.

To appreciate the impact of NQE on the shielding tensors of different nuclei, Fig. 4.13 shows the PIMD to MD ratio of the ensemble averages of the isotropic nuclear magnetic shielding σ and also of the anisotropy Δ. The ratios are shown both for CC and HF results based upon the CC trajectory. The first observation is that CC and HF levels of theory agree qualitatively in the direction (i.e. shielding/deshielding) of NQE shifts. The main quantitative difference between CC and HF is for the carbonyl group in formaldehyde, which is known to exhibit large correlation corrections to the shielding [124]. Regarding the "peripheral" hydrogens, CC and HF results of the CC-PIMD trajectory both agree that NQE lead to a deshielding of 0.5 ppm. While HF also predicts a similar deshielding for the shared proton, CC does not as previously mentioned. This highlights the importance of including *both* electron correlation effects if one is interested in a quantitative assessment of NQE-induced shifts, as both effects in many cases can have cause the same shift but in the opposite directions, canceling each other out. Another important observation in Fig. 4.13 is that NQE shifts in σ are most strongly exhibited at the carbonyl group of formaldehyde, not at the hydrogen atoms. This in fact can also be explained by the quantum-delocalized nature of the shared proton itself, as it polarizes the mobile π-electrons of the carbonyl group during its excursions, leading to such strong shifts in PIMD relative to MD. So far our discussion was focused on σ, but another

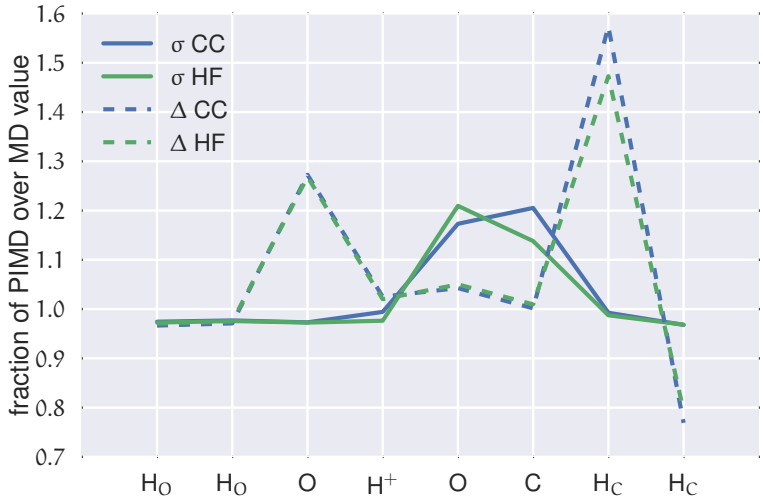

Figure 4.13: Impact of nuclear quantum effects on the isotropic nuclear magnetic shielding σ and the anisotropy Δ in dependence of the level of theory. The lines are to guide the eye.

interesting aspect also shown in Fig. 4.13 is the contrast between σ and Δ. Again, CC and HF provide the same picture for the impact of NQEs on Δ, in fact the agreement here is even better than with σ, with the only sizable difference being in the formaldehyde hydrogens. However, compared to σ, NQEs are far more pronounced on the water oxygen and the formaldehyde, and far less pronounced on the carbonyl atoms. This means that even if NQEs exhibit only a modest shift on σ, this might be due to a cancellation of sizable but opposing shifts in the principal components of the shielding tensor. These findings are particularly significant in solid state NMR, or when one is interested in the shielding anisotropy e.g. in NMR relaxation.

Similarly, the impact of the correlation on the isotropic nuclear magnetic shieldings can be investigated by showing the ratio of the isotropic nuclear magnetic shielding calculated with the CC theory and calculated on the HF level of theory in Fig. 4.14. In general, the correct treatment of correlation effects with CC theory leads to a slightly increase of the isotropic magnetic nuclear shieldings for the neutral parts of the system. For the C–O double bonding the isotropic magnetic nuclear shielding is heavily overestimated for the carbon atom and slightly underestimated for the oxygen atom. Both estimates are slightly reduced with including NQE, which indicates that the NQE and correlation correction effect similarly the

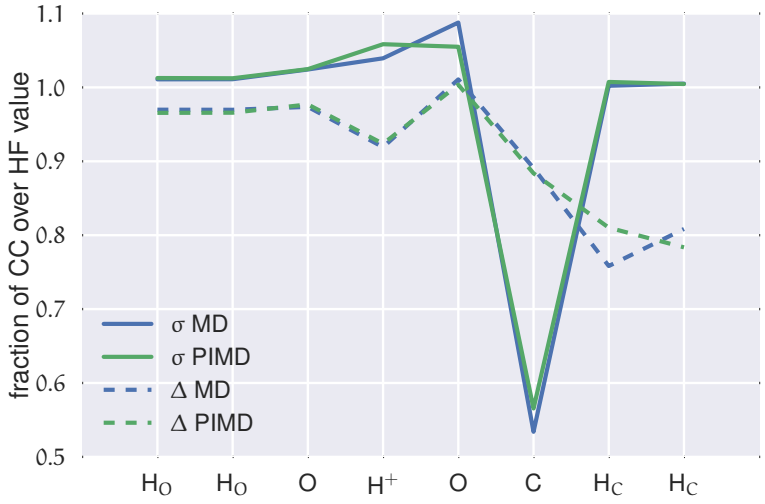

Figure 4.14: Impact of the level of theory on the isotropic magnetic nuclear shielding σ and the anisotropy Δ in dependence of nuclear quantum effects. The lines are to guide the eye.

shieldings. Yet as the NQE are only slightly reduced, a correct treatment of the correlation is absolutely necessary and emphasized.

The isotropic nuclear magnetic shielding of the covalently bound hydrogens either to the oxygen or to the carbon have a striking linear relationship to their distance from the bound nucleus. In Fig. 4.15, a linear fit has been added to guide the eye and to see the linear trend. The linear fit of the hydrogen bound to the oxygen hits the peak of the carbon, so that it is not clear in the classical simulation, if a single linear fit is enough to describe the isotropic nuclear magnetic shielding for all covalently bound hydrogens. Only in the quantum simulation, it is clear that both shieldings are transitioning into each other, but with a different slope.

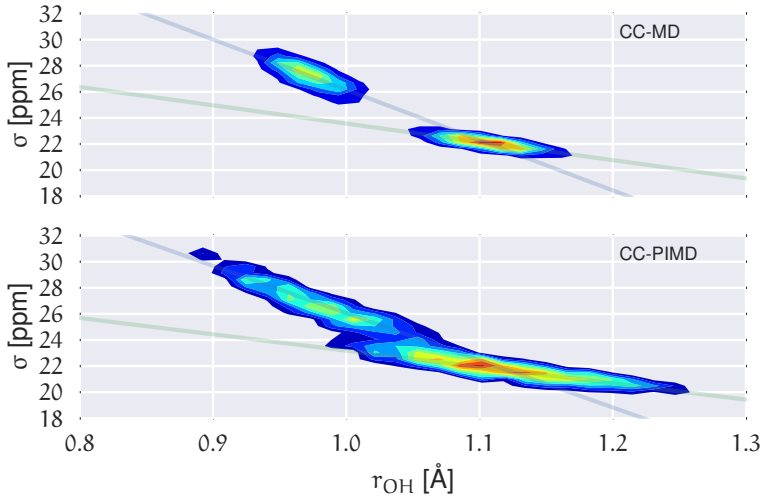

Figure 4.15: Distribution of the isotropic nuclear magnetic shielding σ of all four covalently bound hydrogens in units of ppm in dependence of the oxygen–hydrogen distance r_{OH}. The oxygen (left peak) and carbon bound hydrogens (right peak) are clearly separated and distinguishable. A linear fit has been added to guide the eye.

4.4 CONCLUSIONS

In this chapter, it was shown that the CC-based path integral molecular dynamics technique can be sped up by by providing an initial guess to the cluster and $\hat{\Lambda}$ amplitudes that is already close to the final solution thereof. Furthermore, it is possible to use an approximate solution of the cluster amplitudes that introduces barely visible deviations from the fully converged solution. The computational cost from obtaining the cluster amplitudes is now reduced with this accelerated *quantum molecular dynamics* simulation, which can now be routinely applied. As application, the asymmetric environment of a proton bound between a water and a formaldehyde was investigated and have shown that sampling the additional degrees of freedom of the quantum simulation was absolutely necessary to describe the asymmetric bonding of the proton between the oxygens of the water and the formaldehyde. The computational cost of this calculation could be reduced by about 38.8% with this new approach and allows eventually for the unambiguous quantification of the contribution of finite temperatures by comparing the usual CC-based nuclear magnetic shielding tensor calculations by the ensemble average of the CC-MD trajectory and

furthermore of nuclear quantum effects at this finite temperatures to NMR by comparing the ensemble averages of the CC-PIMD trajectory with the CC-MD ensemble averages.

In the future, this new extrapolation technique would reduce the computational demands even more by extrapolation of the cluster and $\hat{\Lambda}$ amplitudes of density fitted coupled cluster (DF-CC [125]). This has the advantage that the memory limiting integrals are not calculated and saved to disk like in the current simulation but estimated with an auxiliary basis set. This way less computational time is spent in the integral evaluation and our extrapolation scheme may save an ever bigger fraction of the computational cost of future CC-PIMD simulations and will make new applications possible.

Part III

METHOD DEVELOPMENT OF QUANTUM RING CONTRACTION

5

QUANTUM RING CONTRACTION WITH A DELTA POTENTIAL

As already discussed in Sec. 2.2.1, path integral simulations typically are P times computationally more demanding than a classical simulation. In this chapter, this computational cost is reduced significantly by approximating the potential energy surface by a sum of a lower (computationally less demanding) level of theory and the difference thereof with the original one. In real time, this approximation is known as the multiple time step algorithm from Sec. 2.1.2, whereas in (imaginary) path integral simulations a similar relation can be defined. The ring contraction scheme is then used to avoid the need to call the computational expensive potential as often as before because the difference potential is evaluated on a smaller ring polymer with P' beads instead. This results in a theoretical speed-up of $\frac{P'}{P}$ given that the potential at the lower level of theory is of negligible computational complexity. As the total potential cannot be split naturally into separate time scales [67], this approach with the difference potential simplifies the choice on how to split the total potential. Furthermore, it is also applied in a multiple time step algorithm in this work. Previously, other research groups have used a similar splitting in real time only. Anglada *et al.* used a short-range minimal basis set and the non-self-consistent Harris functional to estimate the well converged potential [126]. Guidon *et al.* have been approximated an hybrid DFT functional with a local functional. Luehr *et al.* have calculated the fast varying force of a water cluster either by a sum of independent force calculations of each water molecule in the gas phase, with an empirical Lennard-Jones and Coulomb potential or with a truncated Coulomb operator that effectively restricts the interatomic potential to short ranges [67]. However in this chapter, the computational demanding CC-based electronic structure calculation is approximated with the underlying HF theory. This way, the CC-based calculation is split into the HF and correlation contribution, which is more alike to

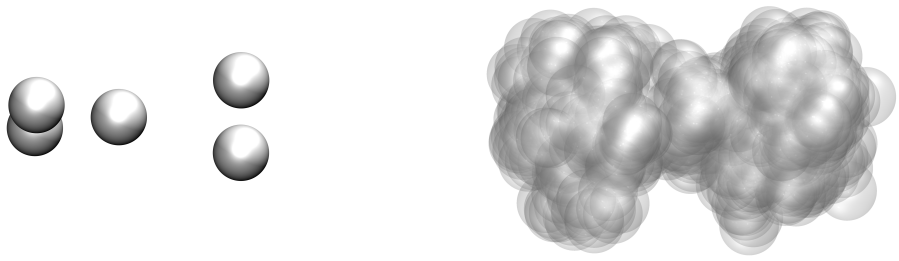

(a) classical simulation (CC-MD) (b) quantum simulation (CC-PIMD)

Figure 5.1: Representative snapshots of H_5^+ with the CC-MD and CC-PIMD simulations.

Ref. [127], where the correlation contribution was approximated with second order Møller-Plesset perturbation theory (MP2). In addition to that, the HF and correlation contribution can be directly used to derive a MTS algorithm with the Liouville formalism from Sec. 2.1.1 in a path integral molecular dynamics simulation. To our best knowledge, this is the first MTS application in real and imaginary time in concert.

This new approach is applied to H_5^+ at low temperatures, where huge NQE and a high number of beads P are expected due to the light atoms and low temperatures. Representative snapshots of the CC-MD and CC-PIMD simulations in Fig. 5.1 immediately show these dramatic delocalization of all particles, which will be discussed in detail after the introduction of the difference or delta potential that includes the correlation contribution of the interatomic potential and the derivation coupled with a MTS algorithm.

5.1 DEFINITION OF THE DELTA POTENTIAL

In a previous work, John *et al.* have defined the delta potential by modifying the full interatomic potential in between the ring polymers from Eq. 2.19 [56]. The main idea is to add and subtract an approximate potential V^{approx} at a lower and compu-

tationally less demanding level of theory to the original *ab initio*-based interatomic potential V^{AI} to obtain the new potential V^{full}

$$\sum_{j=1}^{P} V^{full}(\mathbf{x}_1^{(j)},\ldots,\mathbf{x}_N^{(j)}) = \sum_{j=1}^{P}\Big(V^{AI}(\mathbf{x}_1^{(j)},\ldots,\mathbf{x}_N^{(j)}) + \underbrace{V^{approx}(\mathbf{x}_1^{(j)},\ldots,\mathbf{x}_N^{(j)}) - V^{approx}(\mathbf{x}_1^{(j)},\ldots,\mathbf{x}_N^{(j)})}_{=0}\Big), \tag{5.1}$$

whereas $\mathbf{x}_1^{(j)}$ denotes again the coordinates of the j-th bead of the first particle. This expression is still exact so far as the adding and subtraction of the approximate potential sums up to zero. Yet, it can be sorted into a fast and slowly varying part as

$$\begin{aligned}\sum_{j=1}^{P} V^{full}(\mathbf{x}_1^{(j)},\ldots,\mathbf{x}_N^{(j)}) &= \underbrace{\sum_{j=1}^{P'}\Big(V^{AI}(\mathbf{x}_1^{(j)},\ldots,\mathbf{x}_N^{(j)}) - V^{approx}(\mathbf{x}_1^{(j)},\ldots,\mathbf{x}_N^{(j)})\Big)}_{\text{slowly varying}} \\ &\quad + \underbrace{\sum_{j=1}^{P} V^{approx}(\mathbf{x}_1^{(j)},\ldots,\mathbf{x}_N^{(j)})}_{\text{fastly varying}} \\ &= \sum_{j=1}^{P'} V^{\Delta}(\mathbf{x}_1^{(j)},\ldots,\mathbf{x}_N^{(j)}) + \sum_{j=1}^{P} V^{approx}(\mathbf{x}_1^{(j)},\ldots,\mathbf{x}_N^{(j)}),\end{aligned} \tag{5.2}$$

where the slowly varying part of the potential is a difference between the true ground state and an approximate potential energy surface — the delta potential V^{Δ}. Each part can be evaluated with a different number of beads as the slowly varying part is converged with a lower number of beads [45, 46]. This way the computational more demanding potential V^{AI} is calculated $\frac{P'}{P}$ less often than in a full calculation. If the approximate potential V^{approx} is of negligible computational cost this would result in a speed-up of $\frac{P}{P'}$. When the approximative potential is close enough to the *ab initio*-based one, this approach separates mathematically the time scales of the system whereas only the slowly varying difference potential needs to be calculated at every n_{mts} time step. Fig. 5.2 shows the above equations in a pictographical way.

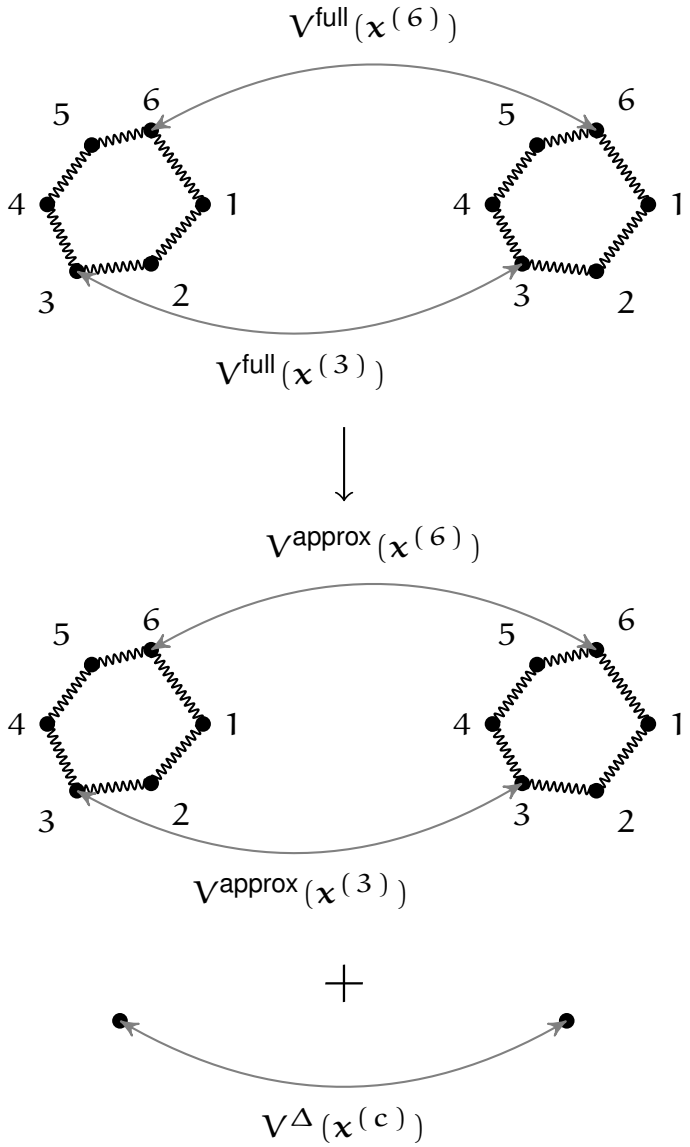

Figure 5.2: Example of the quantum ring contraction of a system consisting of two particles denoted by two ring polymers with 6 beads each. The full potential V^{full} of the two particles is approximated by the sum of the modified potential V^{approx} on all beads and the delta potential on the centroids $V^{(c)}$.

5.2 COMBINATION WITH MULTIPLE TIME STEP ALGORITHM

In this work, a time reversible integration scheme is furthermore presented. In analogy to the splitting of the potentials, the derivative of the potentials can also be split into a fast and slowly varying part. Both, the fast $\mathbf{F}^F$ and slowly varying force $\mathbf{F}^S$ can be inserted in the Liouville formalism from Sec. 2.1.2 and the Liouville operator reads as

$$iL = \sum_j^{NP} \dot{\mathbf{x}}_j \frac{\partial}{\partial \mathbf{x}_j} + \sum_j^{NP} \mathbf{F}_j^F \frac{\partial}{\partial \mathbf{p}_j} + \sum_j^{NP} \mathbf{F}_j^S \frac{\partial}{\partial \mathbf{p}_j} \tag{5.3}$$

$$= \sum_j^{NP} \dot{\mathbf{x}}_j \frac{\partial}{\partial \mathbf{x}_j} + \sum_j^{NP} \mathbf{F}_j^{approx} \frac{\partial}{\partial \mathbf{p}_j} + \sum_j^{NP} \mathbf{F}_j^{\Delta} \frac{\partial}{\partial \mathbf{p}_j}, \tag{5.4}$$

with the delta force $\mathbf{F}_j^{\Delta} = \mathbf{F}_j^{AI} - \mathbf{F}_j^{approx}$ as the difference between the *ab initio* and the approximate force. This delta force can be approximated by using the ring contraction scheme [45, 46] and one obtains

$$iL \approx \sum_j^{NP} \dot{\mathbf{x}}_j \frac{\partial}{\partial \mathbf{x}_j} + \sum_j^{NP} \mathbf{F}_j^{approx} \frac{\partial}{\partial \mathbf{p}_j} \tag{5.5}$$

$$+ \sum_j^{NP} \sum_{j'}^{P'} \frac{P}{P'} T_{jj'} (\mathbf{F}_{j'}^{AI} - \mathbf{F}_{j'}^{approx}) \frac{\delta}{\delta \mathbf{p}_j}$$

$$= iL_x + iL_p^S + iL_p^{\Delta}. \tag{5.6}$$

So far, this scheme is only reformulation of the quantum ring contraction scheme by John *et al.*. Yet, as the delta potential is slowly varying by definition, this splitting of the Liouville operator can be inserted into the multiple time step integrator derivation from Eq. 2.15

$$\begin{aligned} \Gamma(t + \Delta T) = {} & e^{iL_p^{\Delta} \Delta T/2} \\ & \times \left(e^{iL_p^F \delta T/2} e^{iL_x \delta T} e^{iL_p^F \delta T/2} \right)^{n_{mts}} \\ & \times e^{iL_p^{\Delta} \Delta T/2} \Gamma(t). \end{aligned} \tag{5.7}$$

In addition to the reduction of the computational effort in imaginary time with the contraction of the computationally expensive calculation of V^{AI}, the delta force

is only evaluated at each n_{mts}-th time step. The resulting theoretical speed-up will be $n_{mts} \cdot \frac{P}{P'}$. The integration scheme is a mixture of the classical integration scheme from Sec. 2.1.2 and the path integral version in the normal mode representation [128], which becomes clear when inserting the previous splitting of the Liouville operator into Eq. 2.15. The resulting multiple time step integrator is similar to the one from Code 2.2 and straightforward to apply for the path integral extension.

In the following, the computational expensive potential will be calculated with the coupled cluster singles and doubles method with perturbed triples CCSD(T) and HF is used as the approximate potential. Because of the much higher scaling with respect to the system size N of the CC calculation of $\mathcal{O}(N^7)$ in comparison to $\mathcal{O}(N^4)$ for the HF calculation, the latter can be carried out at a more less computational cost. They only sum up when a large number of beads is needed to converge the nuclear Schrödinger equation as then there are many HF calculations to be done.

5.3 NUCLEAR QUANTUM EFFECTS OF H_5^+ AT LOW TEMPERATURES

The following CC-MD and CC-PIMD simulations were performed in the canonical NVT ensemble at 10 K using a discretized time step of 0.5 fs for 25 ps using a modified version of i-PI [92], whereas the forces were calculated at the CCSD(T)/cc-pVTZ level of theory [83, 84, 91, 94, 95, 129] using the CFOUR program package [97, 98]. With $P = 192$ beads, the nuclear Schrödinger equation is found to be essentially exactly solved and is hence employed throughout. An additional CC-MD simulation with classical nuclei ($P = 1$) has been performed in order to quantify the impact of NQE. The isotropic nuclear shielding of the classical and the quantum simulation has been calculated as an ensemble average over each time 1000 decorrelated snapshots at the CCSD(T)/cc-pVTZ level of theory [99, 100].

This system has been studied briefly previously in a PIMD simulation at 5 K at the density functional level of theory (DFT [130, 131]), but was found to yield a qualitatively different structure from correlated calculations [132–135]. Whereas the former incorrectly predicts a symmetric shared proton in between two hydrogen dimers, the latter predicts an H_2 and a slightly separated H_3^+ molecule instead. The well separated H_2 and H_3^+ core can also be seen in the classical CC-MD simulation in Fig. 5.3, where each hydrogen can be found almost stationary at their ground

state distances. At this low temperature it is impossible to overcome the hopping barrier within the classical simulation and the system is separated into a H_2 dimer and a H_3^+ trimer at all times. The hydrogens in the H_2 dimer have a distance of 0.768 Å from each other and the hydrogen dimer in the trimer is separated by about 0.811 Å. The proton has a distance of 0.991 Å and 1.315 Å from the free dimer and dimer in the trimer respectively. The quantum simulation on the other hand results in extreme excursions of all hydrogens. The proton is fully delocalized between the two hydrogen dimers and on average is located in the middle of them with a mean distance of 1.206 Å to all other hydrogens. Due to the proton hopping between both dimers, the H_2 and H_3^+ cores swap and both peripheral hydrogen dimers have now an average distance of 0.808 Å. As shown in Fig. 5.4, the proton in the middle is freely movable and hops between both hydrogen dimers. The spatial distribution in Fig. 5.5, where the right hydrogen dimer is located in the plane of the picture and the left hydrogen dimer sticks out of it, also shows this large excursions of the proton. The movement of the proton in the middle is symmetric to all spatial directions whereas the hydrogen dimers fluctuate predominantly perpendicular to their respective H_2 distances which can be seen especially at the right hydrogen dimer. These extreme excursions can be explained by the increasing quantum delocalizations at lower temperatures which lower the hopping barrier of the proton by including zero-point and tunneling effects. The radius of gyration serves as a measurement of the delocalization which is proportional to $1/\sqrt{T}$ and is given by [16]

$$\begin{aligned} r_G &= \frac{\hbar}{2\sqrt{m_i k_B T}} \\ &= \sqrt{\langle \frac{1}{P} \sum_{j=1}^{P} \left(\mathbf{x}^{(j)} - \mathbf{x}^{(c)}\right)^2 \rangle}, \end{aligned} \tag{5.8}$$

where m_i denotes the mass of particle i. At decreasing temperatures, it expands even to bigger sizes than the average distance of the hydrogen dimers. At the simulated temperature of 10 K, the radius of gyration of the proton in the middle is 1.02 Å and the hydrogens have a mean radius of gyration of 1.35 Å.

To assess the importance of correlation effects, a comparison of the CC-based simulations has been made with HF-based ones. The classical HF-MD simulation already showed similarly to the CC-MD one that the atoms vibrate around the ground state of 0 K. In contrast to DFT, even the HF-MD predicts the correct ground state of

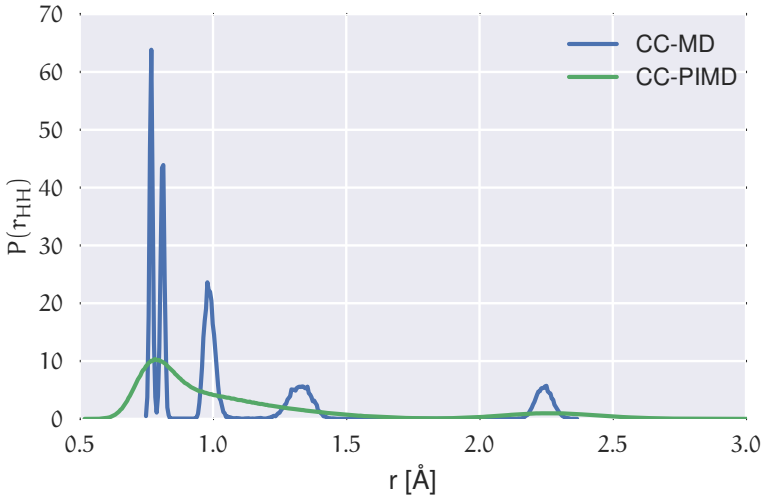

Figure 5.3: Total H–H PCF obtained with CC-MD and CC-PIMD simulations that shows the clear separation of solvation shells in the classical simulation and smearing out of the quantum simulation. The peaks in the CC-MD simulation with increasing distances are sorted as follows: hydrogens in dimer, hydrogens of dimer in trimer, proton in the middle with dimer in trimer, proton in the middle with dimer and both dimers with each other.

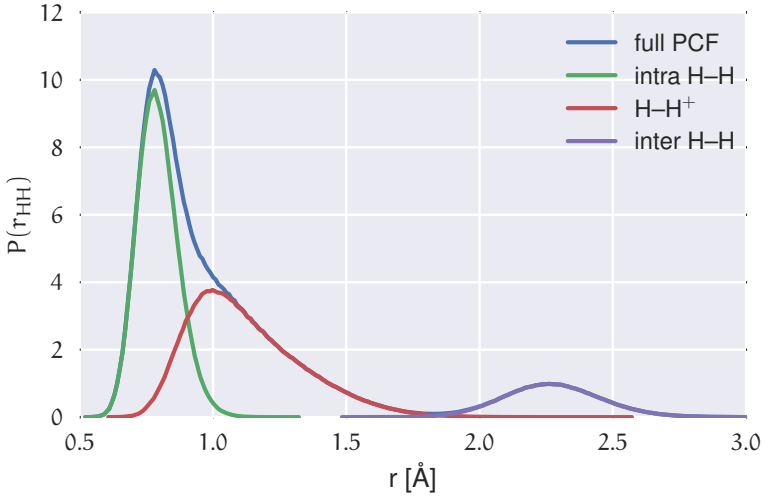

Figure 5.4: Total H–H PCF obtained with the CC-PIMD simulation and the decomposition into the contributions of the intramolecular hydrogen of the dimers (intra H–H), the hydrogens of the dimers with the proton in the middle ($H–H^+$) and intermolecular hydrogen of the dimers (inter H–H).

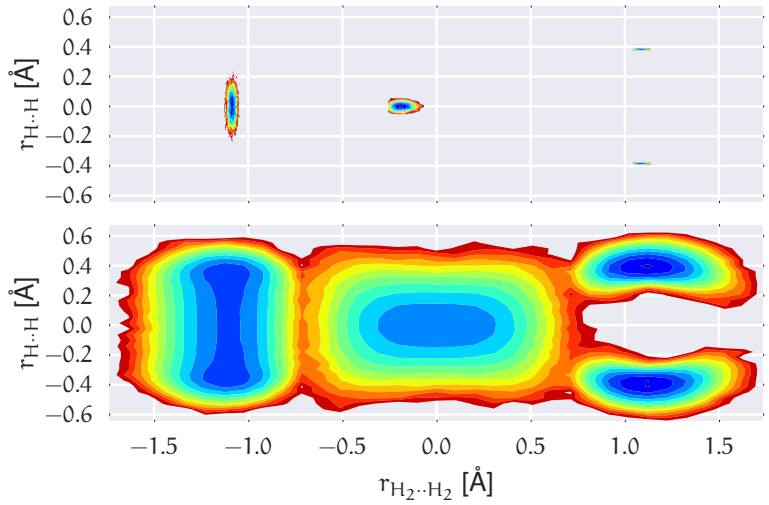

Figure 5.5: Spatial distribution of all atoms in the CC-MD and CC-PIMD simulations across the plane spanned by both center of masses of the hydrogen dimers on the left and right hand side ($r_{H_2\cdot\cdot H_2}$) and the H–H distance of the right hydrogen dimer ($r_{H\cdot\cdot H}$).

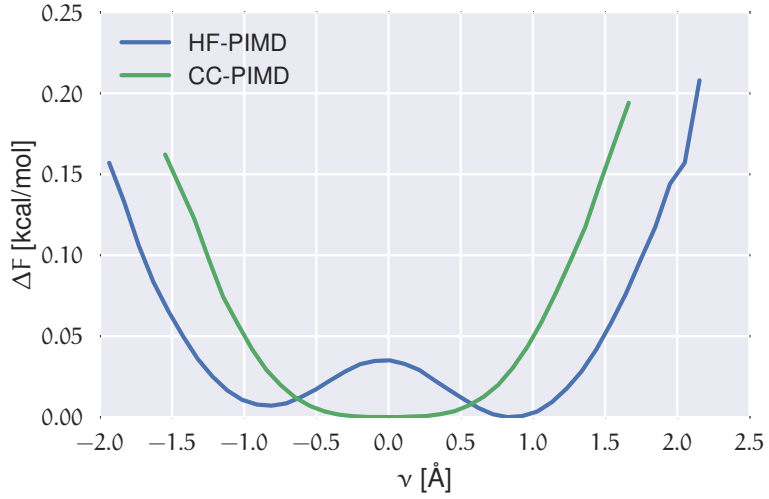

Figure 5.6: Free energy distribution in kcal/mol of the shared proton with respect to the proton reaction coordinate of our CC-PIMD simulation in comparison with a HF-based PIMD simulation.

a well separated H_2 and an H_3^+ molecule. The main difference with and without correlation effects is that the atoms are even more localized in the HF-MD simulation than in the CC-MD simulation, which means that the HF potential is nonphysically steep at the geometric optimum. Nevertheless, with the correct treatment of NQE in the HF-PIMD simulation the proton is able to hop between the other hydrogens in a fashion similar to the CC-PIMD simulation. Yet in the HF-PIMD simulation the proton is prevented to hop as free as in the CC-PIMD simulation and needs to overcome a crossing barrier. This can be seen best in the free energy difference of the proton reaction coordinate ν in Fig. 5.6, where the energy barrier that appears in the HF-PIMD simulation is estimated to about 0.035 kcal/mol. To conclude this assessment, the electronic correlation needs to be carefully and accurately sampled to correctly describe the quantum system qualitatively and quantitatively.

To investigate the molecular structure in more detail, the nuclear magnetic shielding tensor is calculated to probe small changes in the geometry. The proton reaction coordinate of this system is defined as the difference of the distances of the proton to the centers of the peripheral hydrogen dimers $\nu = r_{H_{2,\text{left}}} - r_{H_{2,\text{right}}}$ and plotted against the isotropic magnetic nuclear shielding tensor of the proton in the middle in Fig. 5.7. A clear dependency of the reaction coordinate can be seen, which is in the quantum simulation very similar in shape to the proton reaction coordinate from Chapter 3 in Fig. 3.3. Even though the average isotropic magnetic nuclear shielding of the proton increases only slightly due to the NQE from 10.8 ppm to 11.2 ppm, the shape of the instantaneous isotropic magnetic nuclear shielding changes dramatically due to the large excursions of the proton. At the same time, the average isotropic magnetic nuclear shieldings of the other hydrogens is decreasing slightly from 23.0 ppm in the classical simulation and to 22.8 ppm in the quantum simulation and an almost linear dependency on the approaching of the proton is seen in Fig. 5.8, where only the isotropic nuclear magnetic shieldings of the left hydrogen dimer is ploted so that $\nu > 0$ implies that the proton approaches the left hydrogen dimer and departs the right hydrogen dimer. In the limit of a large values of the proton reaction coordinate ν, which means that the proton is very close to the hydrogen dimer at the left hand side, the isotropic magnetic nuclear shielding of the proton approaches the one of the hydrogens in the left hydrogen dimers. The distributions of the isotropic nuclear magnetic shieldings overlap in the quantum simulation and are shown in Fig. 5.9. This crossing of of the isotropic magnetic nuclear shieldings has already be indicated in the spatial distributions in

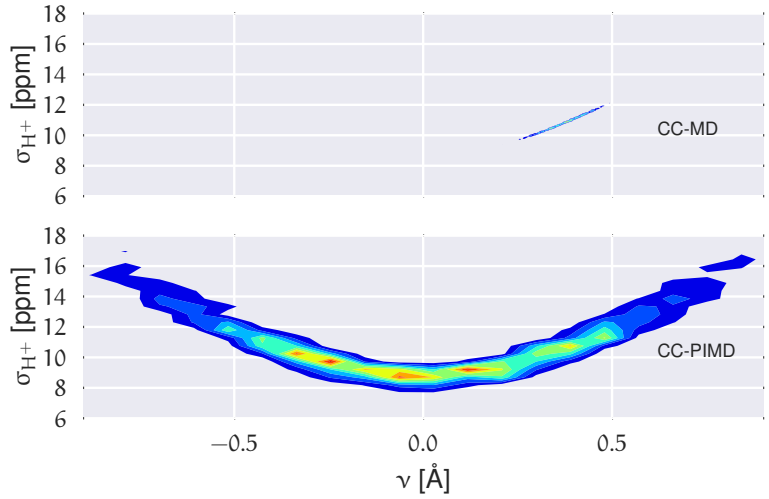

Figure 5.7: Distribution of the isotropic magnetic nuclear shielding σ of the proton vs proton reaction coordinate ν in the CC-MD and CC-PIMD simulations.

Fig. 5.5, where the distributions of the proton and the other hydrogens clearly overlap. Nevertheless, it was not observed that such a crossing actually happens which would need to happen in all beads at a similar time, which is due to the extreme delocalization a very unlikely event.

5.3.1 *Limit of contracted ring polymer with* $\lim_{P'\to 1} P'$ *beads*

In this section, the contraction scheme outlined above will be investigated to speed up the CC-PIMD calculation of the H_5^+ system. Moreover, the scaling behavior of the quantum ring contraction approach with the delta potential is assessed and the resulting trajectory is directly compared to the one of the fully converged CC-PIMD simulation. As an approximate potential, the Hartree-Fock potential was chosen. This is consistent with the usual calculation procedure of the total energy that is usually separated into the HF energy and correlation energy, which is calculated with a so-called post-HF method. The naïve approach would be to directly contract the delta potential in Eq. 5.5 directly to $P' = 1$ which was found to be not possible with this kind of system and the reasons thereof are now outlined in the following. In the spatial distribution in Fig. 5.5, it can be seen that each hydrogen dimers are separated by about 0.8 Å on average, which is not the case for a contracted ring

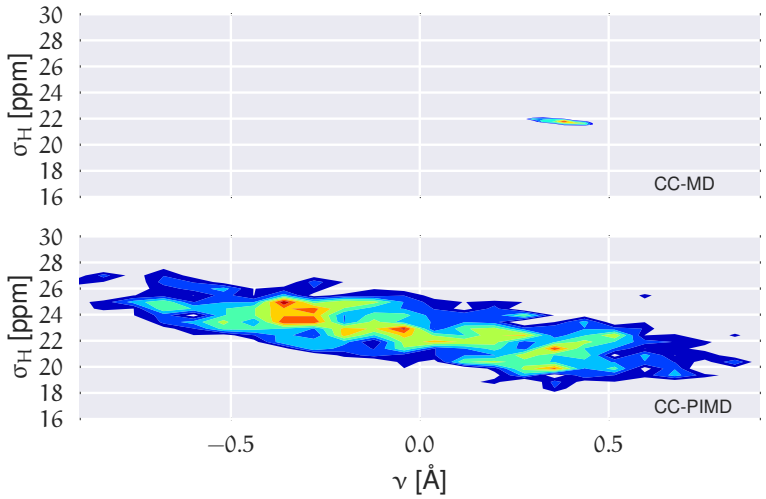

Figure 5.8: Distribution of the isotropic magnetic nuclear shielding σ of the hydrogens vs proton reaction coordinate ν in the CC-MD and CC-PIMD simulations.

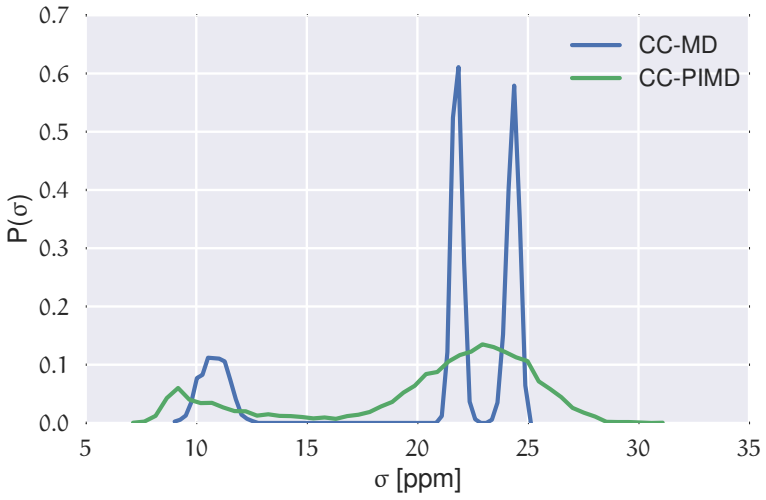

Figure 5.9: Distribution of the isotropic magnetic nuclear shielding σ of all particles. The first peak is the isotropic magnetic nuclear shielding of the proton and the other from the other hydrogens. In the CC-PIMD simulation, the distributions of σ of the proton and the other hydrogens do overlap.

polymer. In the previous section, it was already seen that the radius of gyration of the hydrogens in the hydrogen dimers at the end of the H_5^+ complex is by about 70%, which can lead to the intertwining of the hydrogen dimers' ring polymers. In this case, the centroids are too close to each other and the electronic structure calculation cannot be carried out anymore because of the steep scaling of the nuclear repulsion. Most electronic structure codes restrict the distances to a predefined value, which is 0.3 Å in the case of the CFOUR program package [98]. As the centroid density has no physical meaning [136–139], this can not be easily circumvented. To find the minimal possible bead contraction in the limit of $\lim_{P'\to 1} P'$, the minimum, average and maximum distances between the intramolecular H_2 are calculated in the contracted systems. This is done by retracing and contracting the CC-PIMD simulation to P' beads and calculating the H_2 distances in this contracted system. Fig. 5.10 shows these minima, averages and maxima with respect to P'. It can be seen that the average distance of the hydrogen dimers is approximate constant from about $P' = 20$ to higher P' values, whereas the minimum is almost linear in that range. At a bead contraction number of $P' = 20$ a minimum of slightly above 0.3 Å is reached and taken as the minimal possible contraction value. As the ring polymer is contracted from $P = 192$ to $P' = 20$, so that the CC-based potential is only evaluated 20 times per time step instead of 192 and the HF-based potential is evaluated on the full ring polymer with negligible computational cost, this results in a theoretical speed-up of 9.6. In practice and in this specific example, the CC calculation is about four times more computationally demanding and a total speed-up of 2.6 is obtained in practice. The computational efficiency will be further improved with combining this algorithm with a MTS algorithm in the next section.

The efficiency of this approach to approximate the full potential energy surface at a lower level of theory and the slowly varying delta potential V^Δ is inspected by decomposing the H–H PCF into their different contributions.To compare the impact of the approximation to only evaluate the delta potential on a contracted number of beads, the PCF of both (the approximate and the fully converged) simulations are shown in Fig. 5.11. The first and last solvation shell of the intramolecular and intermolecular hydrogen is almost identically and vanishing. The biggest difference between those two calculations can be found in the second solvation shell, the distribution of the hydrogens of the dimers with the proton in the middle.

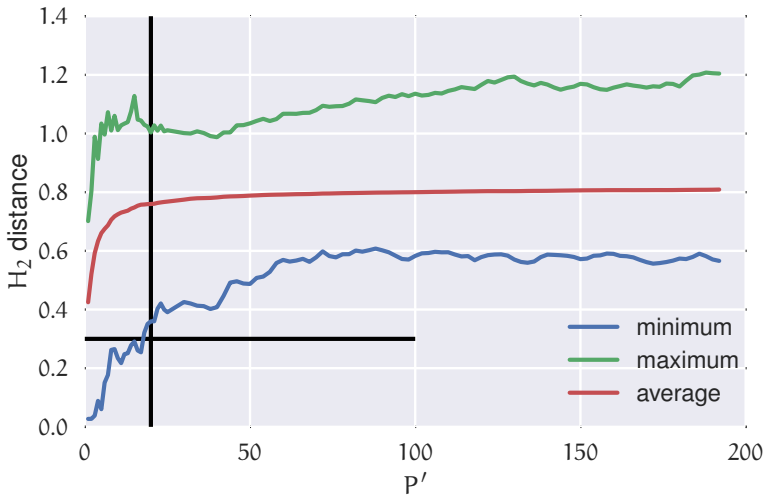

Figure 5.10: Minimum, average and maximum distances between the intramolecular H_2's as a function of the contracted bead number P' in the CC-PIMD simulation. For details see text and Eq. 5.5. The horizonal line is drawn at a hydrogen dimer distance of 0.3 Å and the vertical at $P' = 20$.

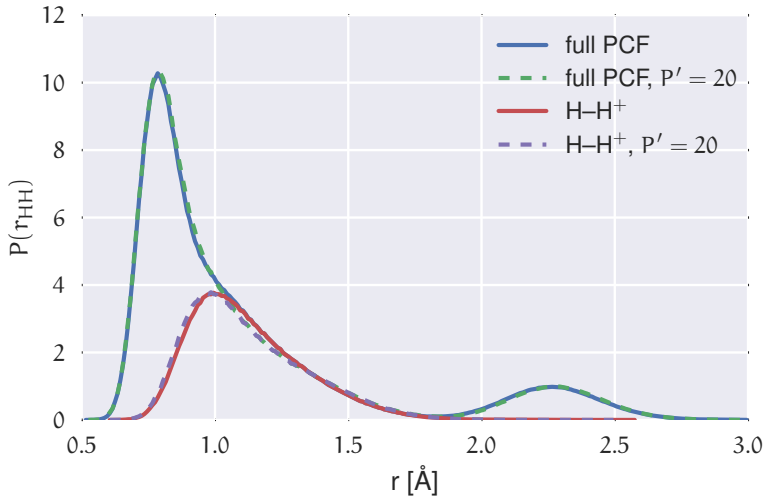

Figure 5.11: Total H–H PCF obtained with the full CC-PIMD simulation and the one with quantum ring contraction employed and the decomposition into the contributions of the intramolecular hydrogen of the dimers (intra H–H), the hydrogens of the dimers with the proton in the middle ($H–H^+$) and intermolecular hydrogen of the dimers (inter H–H).

5.3.2 *Combination of the Quantum Ring Contraction Scheme with a Delta Potential with the Multiple Time Step Algorithm*

In this section, the quantum ring contraction scheme with the delta potential of the previous section is combined with the multiple time step algorithm to save additional computational time and still sampling the potential energy surface of the original highly demanding and accurate level of theory. In the previous section, the delta potential was defined as the correlation contribution of the coupled cluster potential and was contracted to a smaller ring polymer to gain computational efficiency. In addition to that the same slowly varying delta potential can be used in a MTS scheme outlined already in the Sec. 5.2 to reduce the computational demands even further. With $n_{mts} = 5$, the interatomic potential at the CC level of theory is then only evaluated on 20 beads at each 5-th time step, whereas in the full CC-PIMD simulation it was evaluated 192 times in each time step. Instead on each of the 192 beads in each time step the HF potential needs to be calculated. This corresponds to a theoretical speed-up of 48, which can only be reached in when the CC calculation has such a big computational effort that the HF calculation can be treated as negligible. In practice and in this specific example, the CC calculation is about four times more computationally demanding than the HF one. This implies that the maximum reachable speed-up is also four [140]. In practice, a total speed-up of 3.6 is obtained with this new approach, which is 90.6% of the maximum reachable value.

The efficiency of this approach is now compared with and without MTS employed in Fig. 5.12. Both simulations are found to be nearly indistinguishable, which shows that the multiple time step algorithm can be straightforwardly applied in conjunction to the quantum ring contraction with a delta potential.

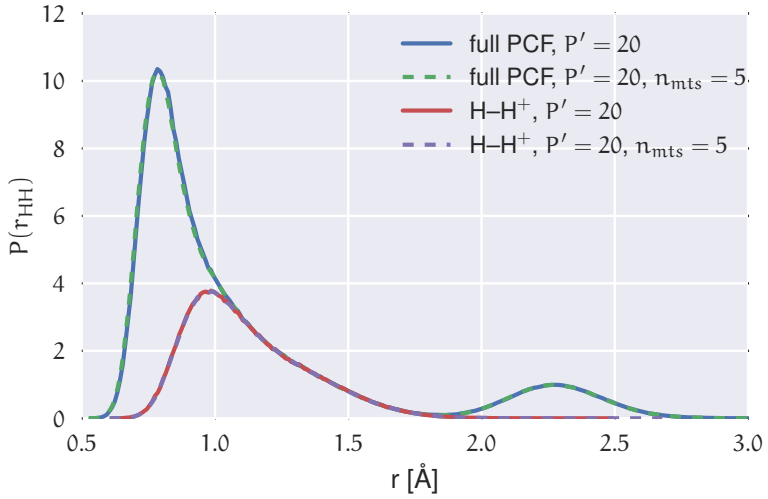

Figure 5.12: Total H–H PCF obtained with the contracted CC-PIMD simulation and the one with MTS employed and the decomposition into the contributions of the intramolecular hydrogen of the dimers (intra H–H), the hydrogens of the dimers with the proton in the middle (H–H^+) and intermolecular hydrogen of the dimers (inter H–H).

5.4 CONCLUSIONS

In this chapter, a computational very demanding *quantum molecular dynamics* simulation at low temperatures has been carried out and therefore was accompanied with an high number of beads. With the quantum ring contraction scheme with the delta potential, defined as difference between CC and HF theory, a theoretical speed up of 9.6 can be achieved, if the HF calculation is assumed to be of negligible computational cost. Together with a MTS scheme, with which the computational demanding delta potential is only evaluated at every fifth time step, no visible approximations have been noted at the full pair correlation functions. The total speed-up that can be achieved with this hybrid quantum ring contraction and multiple time step approach is 48. To our knowledge, we note that this is the first simulation that combines a ring contraction scheme (in imaginary time) with a multiple time step in real time.

The correlation effects of both, the electronic and the quantum nuclear degrees of freedom were found to be of enormous importance and need to be carefully and accurately sampled to correctly describe the system qualitatively and quantitatively.

In the classical CC-MD simulation, the investigated H_5^+ system was found almost at the ground state of a geometric optimization with a H_2 dimer and a separated H_3^+ trimer. However in the quantum simulation the light hydrogens undergo extreme excursions and the proton in the middle is fully delocalized. The isotropic nuclear magnetic shieldings of the proton and the other hydrogens have been found to show an overlapping distribution in the quantum simulation.

6

QUANTUM RING CONTRACTION WITH DERIVATIVES

In Sec. 2.2, the Hamiltonian of a ring polymer with P beads was given by

$$H_P(\mathbf{x},\mathbf{p}) = \sum_{j=1}^{P}\left[\sum_{i=1}^{N}\frac{\mathbf{p}_i^{(j)2}}{2m_i} + \frac{m_i\omega_P^2}{2}\left(\mathbf{x}_i^{(j)} - \mathbf{x}_i^{(j+1)}\right)^2 + V(\mathbf{x}_1^{(j)},\ldots,\mathbf{x}_N^{(j)})\right], \tag{6.1}$$

where the potential V is evaluated on each of the P beads separately. This is therefore accompanied with a P times greater computational cost. In the previous chapter, the computational demands have been reduced by splitting the potential into a slowly and fast varying part. The slowly varying one can be approximated by calculating the interatomic potential on a smaller, contracted ring polymer and expanding the potential to the full ring polymer with the ring contraction scheme (see Refs. [45, 46] and Sec. 2.2.1). This has been applied by defining an appropriate delta potential in the previous Chapter 5. In this chapter, another possibility to approximate the potential is explored. Instead of contracting just one contribution to the interatomic potential to a smaller ring polymer, the full potential is contracted and further derivatives are calculated of this contracted ring polymer. These are incorporated into an extended ring contraction (and expansion) scheme that is closer to the full potential and improves upon solely using the potential of the contracted ring polymer in the expansion scheme. This idea is independent of the splitting of the potential into several parts and can be applied straightforwardly for any analytic potential.

In the following, this extended version of the standard ring contraction scheme is motivated starting from simpler, stricter conditions which are then removed in a step wise fashion that ultimately leads to the final algorithm. The convergence of

this approach is benchmarked against the protonated water dimer from Chapter 3 that was already investigated in detail. The efficiency is also compared to other convergence acceleration methods such as a quantum thermostat [141, 142].

6.1 EXTRAPOLATION WITH TAYLOR POLYNOMIAL

The centroid or center of mass $\mathbf{x}^{(c)} = \frac{1}{P}\sum_{j=1}^{P}\mathbf{x}_i^{(j)}$ is used as a starting point to derive a new approach to include derivatives in the ring polymer contraction scheme. It is equal to the (single) bead of a contracted ring polymer with $P' = 1$ from Eq. 2.24. Derivatives of the interatomic potential at the centroid can now be efficiently with a Taylor polynomial of this center of mass. Thus, this new extended version of the ring polymer contraction scheme is designed to contain the standard ring polymer contraction scheme. For the total potential in Eq. 6.1, the Taylor polynomial reads as

$$V_{\text{total}}(\mathbf{x}) = \sum_{j=1}^{P} V(\mathbf{x}^{(j)}) = \sum_{j=1}^{P}\sum_{n=0}^{N_c}\left(\mathbf{x}^{(j)} - \mathbf{x}^{(c)}\right)^n \frac{V^{(n)}(\mathbf{x}^{(c)})}{n!}, \tag{6.2}$$

where N_c denotes the order of the Taylor polynomial and $V^{(n)}(\mathbf{x}^{(c)})$ is the n-th derivative of the analytic and differentiable potential V with respect to the argument — in this case the centroid of the ring polymer. All potentials on the beads of the system are now approximated with the potential and derivatives thereof with respect to the centroid proportionally to the distance vector of the bead from the centroid. Instead of contracting to the centroid and therefore to a one-bead system, this expression can be extended for an arbitrary contracted ring polymer with $P' \neq 1$ beads. The Taylor polynomial then takes the form

$$\sum_{j=1}^{P} V(\mathbf{x}^{(j)}) = \sum_{j=1}^{P}\sum_{n=0}^{N_c}\left(\mathbf{x}^{(j)} - \sum_{j'=1}^{P'} T_{jj'}\mathbf{x}^{(j')}\right)^n \frac{1}{P'}\sum_{j'=1}^{P'}\frac{V^{(n)}(\mathbf{x}^{(j')})}{n!} \tag{6.3}$$

$$= \frac{P}{P'}\sum_{j'=1}^{P'} V(\mathbf{x}^{(j')}) \tag{6.4}$$

$$+ \sum_{j=1}^{P}\sum_{n=1}^{N_c}\left(\mathbf{x}^{(j)} - \sum_{j'=1}^{P'} T_{jj'}\mathbf{x}^{(j')}\right)^n \frac{1}{P'}\sum_{j'=1}^{P'}\frac{V^{(n)}(\mathbf{x}^{(j')})}{n!}.$$

The first term in Eq. 6.4 can be readily identified with the standard ring contraction scheme by Markland *et al.* [45, 46] (see also Eq. 2.25). The second term systematically incorporates further corrections of higher-order derivatives of the energy such as the force and hessian proportionally to the difference of the vector of the positions in the full bead and the contracted ring polymer system. When $N_c = 0$, the higher order corrections are not included in the Taylor polynomial and the standard ring polymer contraction is fully retained by construction. It was the aim of this algorithm right from the beginning to include the standard ring polymer contraction scheme as a strict condition. This has the further implication, that this approach is easy to implement in existing path integral molecular dynamics programs as only additional correction terms need to be added to the previous potential estimate. Fig. 6.1 shows this systematic approach in a pictographical way for the case of $P' = 1$.

In addition to including the standard ring contraction scheme, this quantum ring contraction approach with derivatives also contains the correct limit of a full bead calculation. When $P' = P$ the corrections to the total energy is exactly zero as the $T_{jj'}$ transformation in Eq. 6.4 leaves the ring polymer unchanged (see also Eq. 2.23) and the difference vector of the Taylor polynomial evaluates to zero. With other words, the further derivatives do not contribute to the potential when doing a full bead calculation.

In order to obtain an expansion expression for the force, it is necessary to know how the derivative acts on this difference vector of the Taylor polynomial. When the derivative with respect to the full bead system $\nabla_{\mathbf{x}_i^{(j)}}$ acts on contracted ring polymer $\mathbf{x}^{(j')}$, it creates another transformation matrix $T_{j'j}$ that contracts the ring polymer from P beads to P' beads. This reads as

$$\nabla_{\mathbf{x}_i^{(j)}} \left(\mathbf{x}^{(j)} - \sum_{j'=1}^{P'} T_{jj'} \mathbf{x}^{(j')} \right) = \underbrace{\left(1 - \underbrace{\sum_{j'=1}^{P'} \sum_{j=1}^{P} T_{jj'} T_{j'j}}_{1} \right)}_{0} \nabla_{\mathbf{x}_i^{(j)}} \mathbf{x}^{(j)}, \tag{6.5}$$

where the inverse of the $T_{j'j}$ contraction is a $T_{jj'}$ expansion of the ring polymer which applied together leave the ring polymer unchanged. Therefore the derivative of this difference vector evaluates to zero by construction.

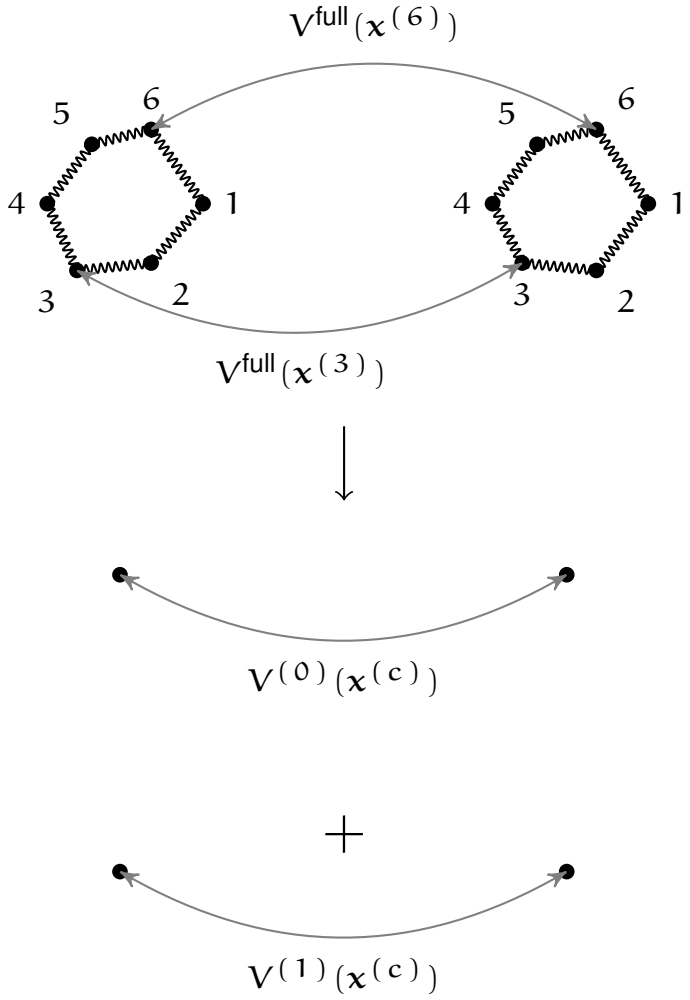

Figure 6.1: Example of the quantum ring contraction of a system consisting of two particles denoted by two ring polymers with 6 beads each. The full potential V^{full} of the two particles is approximated by the Taylor polynomial of the potential $V^{(0)}$ and the derivative extrapolation $V^{(1)}$ on the centroids.

The force acting on the full P-bead system can now be easy calculated by applying the chain rule to extended ring contraction scheme for the potential in Eq. 6.3 which evaluates to

$$
\begin{aligned}
\mathbf{F}_i^{(j)} &= -\nabla_{\mathbf{x}_i^{(j)}} V_{\text{total}} = -\sum_{j'=1}^{P'} T_{j'j} \nabla_{\mathbf{x}_i^{(j')}} V_{\text{total}} \\
&= -\sum_{j=1}^{P} \sum_{n=0}^{N_c} \left(\mathbf{x}^{(j)} - \sum_{j=1}^{P'} T_{jj'} \mathbf{x}^{(j')} \right)^n \frac{1}{P'} \sum_{j'=1}^{P'} T_{jj'} \frac{V^{(n+1)}(\mathbf{x}^{(j')})}{n!} \qquad (6.6) \\
&= \frac{P}{P'} \sum_{j'=1}^{P'} T_{jj'} \mathbf{F}_i^{(j')} \qquad (6.7) \\
&\quad - \sum_{j=1}^{P} \sum_{n=1}^{N_c} \left(\mathbf{x}^{(j)} - \sum_{j=1}^{P'} T_{jj'} \mathbf{x}^{(j')} \right)^n \frac{1}{P'} \sum_{j'=1}^{P'} T_{jj'} \frac{V^{(n+1)}(\mathbf{x}^{(j')})}{n!},
\end{aligned}
$$

where $\mathbf{F}_i^{(j')} = -\nabla_{\mathbf{x}_i^{(j')}} V(\mathbf{x}^{(j')})$ is the force that acts on particle i on the j'-th bead of the contracted system. The first term of the force can again be identified as the standard ring contraction scheme from Eq. 2.26 and further corrections of order up to $N_c + 1$ are added. The order of these corrections is one order higher than the energy expression before. These expressions can be made clear at best when showing the expressions for the harmonic limit $N_c = 1$ which will also be used later in the benchmark calculation of the protonated water dimer.

6.1.1 *Harmonic Limit*

In this section, the extended ring polymer contraction scheme is outlined for simplicity for the one dimensional harmonic potential $V(x) = x^2$. This serves as an initial test case to show the basic features and properties in the harmonic limit, which is then applied in the next section to a real system. Because this potential is a second order polynomial, a Taylor polynomial that approximates the potential converges unsurprisingly at $N_c = 2$, whereas the Taylor polynomial that approximates the force $F(x) = -2x$ already converges with one further derivative of the force, see Figs. 6.2 and 6.3 respectively. This means only $N_c = 1$ is necessary to fully converge the force to the harmonic limit, which is needed to employ an accurate MD simulation. In other words, a Taylor polynomial of order $N_c = 1$ is needed to obtain the correct dynamics in a MD simulation that uses an harmonic potential, but the

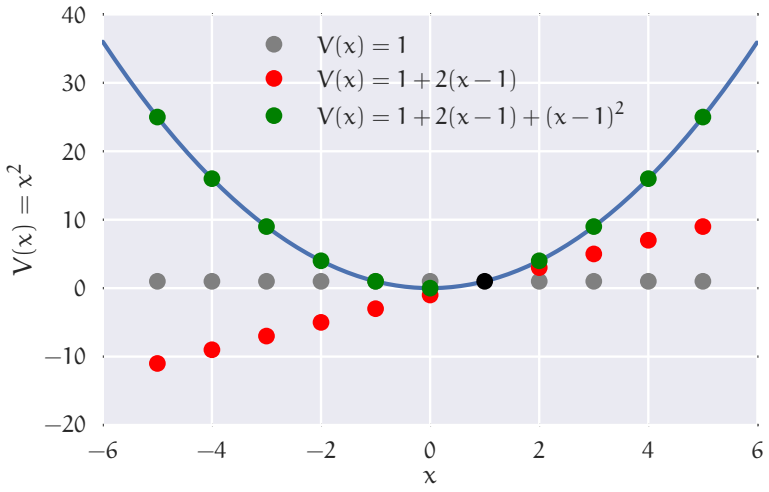

Figure 6.2: The harmonic potential $V(x) = x^2$ is approximated with a second order Taylor polynomial, i.e. the forces and the hessian, at $x = 1$.

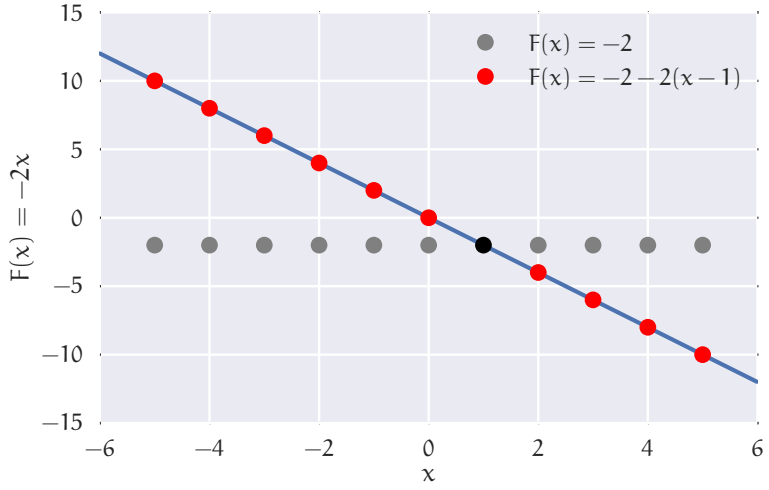

Figure 6.3: The force of the harmonic potential $V(x) = x^2$ is approximated with a first order Taylor polynomial, i.e. only the hessian, at $x = 1$.

potential is not yet fully retained. In this case, the equations for the interatomic potential and the force approximated with the extended ring polymer contraction scheme read as

$$\sum_{j=1}^{P} V(\mathbf{x}^{(j)}) = \frac{P}{P'} \sum_{j'=1}^{P'} V(\mathbf{x}^{(j')}) + \sum_{j=1}^{P} \left(\mathbf{x}^{(j)} - \sum_{j'=1}^{P'} T_{jj'} \mathbf{x}^{(j')} \right) \frac{1}{P'} \sum_{j'=1}^{P'} V^{(1)}(\mathbf{x}^{(j')}) \tag{6.8}$$

$$\mathbf{F}_i^{(j)} = \frac{P}{P'} \sum_{j'=1}^{P'} T_{jj'} \mathbf{F}_i(j') - \sum_{j=1}^{P} \left(\mathbf{x}^{(j)} - \sum_{j=1}^{P'} T_{jj'} \mathbf{x}^{(j')} \right) \frac{1}{P'} \sum_{j'=1}^{P'} T_{jj'} V^{(2)}(\mathbf{x}^{(j')}). \tag{6.9}$$

In addition to that, the expression can be further simplified when contracting to the centroid $P' = 1$ to

$$\sum_{j=1}^{P} V(\mathbf{x}^{(j)}) = P V(\mathbf{x}^{(c)}) + \sum_{j=1}^{P} \left(\mathbf{x}^{(j)} - \mathbf{x}^{(c)} \right) V^{(1)}(\mathbf{x}^{(c)}) \tag{6.10}$$

$$\mathbf{F}_i^{(j)} = \mathbf{F}_i^{(c)} - \left(\mathbf{x}^{(j)} - \mathbf{x}^{(c)} \right) V^{(2)}(\mathbf{x}^{(c)}). \tag{6.11}$$

The potential is approximated by additionally using the gradient of the potential and the forces are approximated additionally using the second derivative of the potential or hessian of the potential. Note however that the second derivative is not directly used to expand the potential of the contracted ring polymer. This was already seen at Eqs. 6.3 and 6.6, where an approximation up to the N_c-th derivative of the potential requires the knowledge of the first $N_c + 1$ derivatives of the interatomic potential $V(\mathbf{x})$.

6.2 RESULTS FOR THE EXAMPLE OF THE PROTONATED WATER DIMER

This new ring contraction scheme is benchmarked on the example of the protonated water dimer which was already investigated in detail at the CCSD level of theory in Chapter 3. Analytic derivatives up to second order are calculated at the CCSD/cc-pVDZ level of theory [91, 93–96, 143–145] using the CFOUR program package [97, 98]. The potential and forces of the full ring polymer is approximated according to Eqs. 6.3 and 6.6 in the harmonic limit with $N_c = 1$ as just described in detail in the previous section. This has been implemented into a preliminary version in i-PI [92] and the total simulated time was 3.4 ps. All other computational details are the same as in Chapter 3 so that the efficiency of this extended ring contraction scheme can be directly compared with those results.

An overview and general comparison of the convergence of the four different methods is shown in Fig. 6.4 for the oxygen–hydrogen pair correlation function (PCF) and in Fig. 6.5 for the hydrogen–hydrogen PCF. The line with $P = 1$ denotes the classical simulation and $P = 32$ the quantum simulation where the Schrödinger equation is found to be essentially exactly solved. Then the O–H stretch in Fig. 6.4 is broadened whereas the height is about cut in one third. From the simulation with $P = 4$ it can be seen that this usual route to convergence of a PIMD simulation by increasing the number of beads of the ring polymer is quite slow. The first method, that approximates the potential and forces of the fully converged simulation, is to just calculate the potential and forces on a smaller ring polymer with P' beads and to expand those results to the bigger ring polymer, which is included in the extended ring polymer contraction with $N_c = 0$. This overestimation of the quantum effects can be seen especially for the case of $P' = 1$ and origins in the smaller radius of gyration of any contracted ring polymer that occurs with the use of the ring contraction scheme and has been investigated in detail in Sec. 5.3.1. Fig. 6.6 shows the exaggerated radius of gyration of all hydrogens in this simulation whereas the radius of gyration of the oxygens is less pronounced due to their higher masses. For instance, in the case of the O–H stretch in Fig. 6.4a the potential is calculated at a further O–H distance and the expanded ring polymer can freely approach to smaller non-physical distances as the nuclear–nuclear repulsion is underestimated. A similar trend can also be seen in the hydrogen–hydrogen PCF in Fig. 6.5, where again mainly the intramolecular hydrogen is benefiting from the anharmonic correction to the total potential. The intermolecular hydrogen is located at bigger

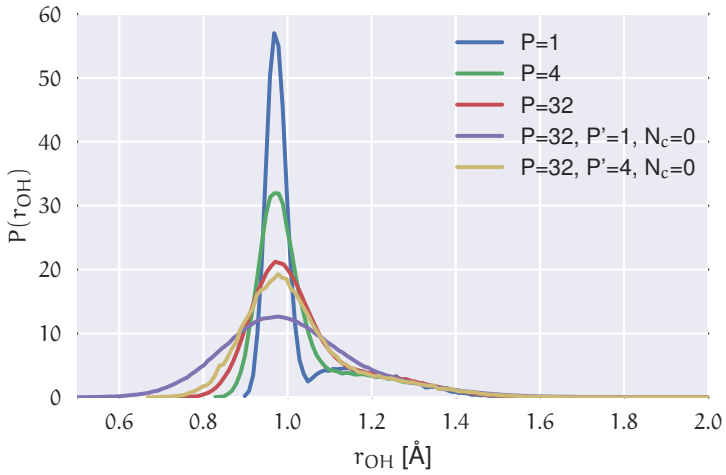

(a) $N_c = 0$ or up to first derivatives

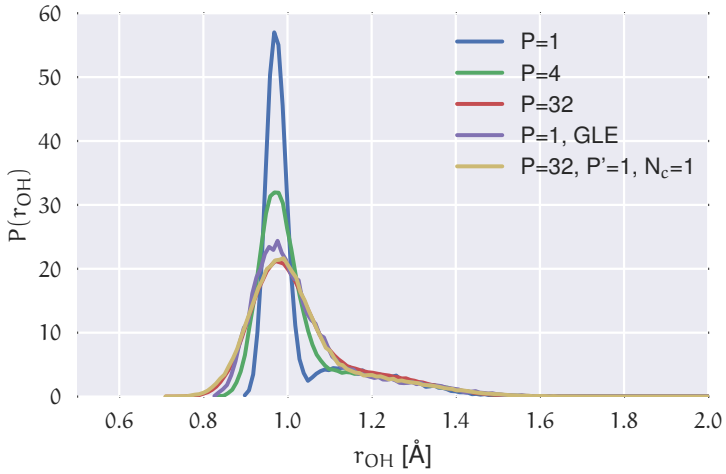

(b) $N_c = 1$ or up to second derivatives

Figure 6.4: Total O–H PCF obtained by CC-MD or CC-PIMD simulations and different expansions of the Taylor polynomial $N_c = 0$ (ring contraction scheme or calculating of up to first derivatives) or $N_c = 1$ (new quantum ring contraction scheme or calculation of up to second derivatives). The convergence is also compared with a CC-MD simulation with a quantum thermostat (GLE).

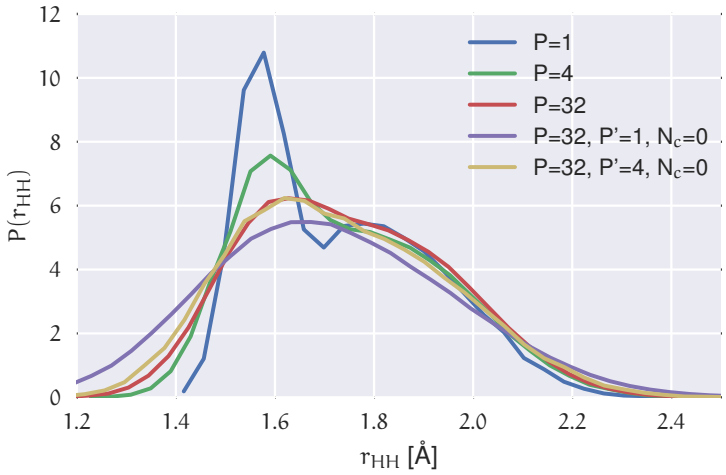

(a) $N_c = 0$ or up to first derivatives

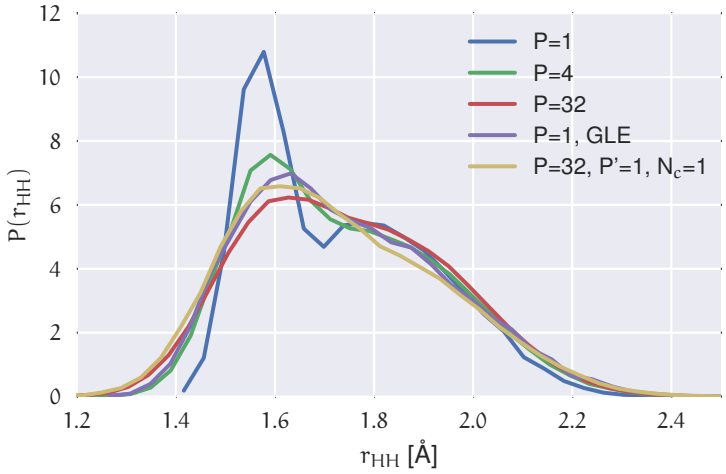

(b) $N_c = 1$ or up to second derivatives

Figure 6.5: Total H–H PCF obtained by CC-MD or CC-PIMD simulations and different expansions of the Taylor polynomial $N_c = 0$ (ring contraction scheme or calculating of up to first derivatives) or $N_c = 1$ (new quantum ring contraction scheme or calculation of up to second derivatives). The convergence is also compared with a CC-MD simulation with a quantum thermostat (GLE).

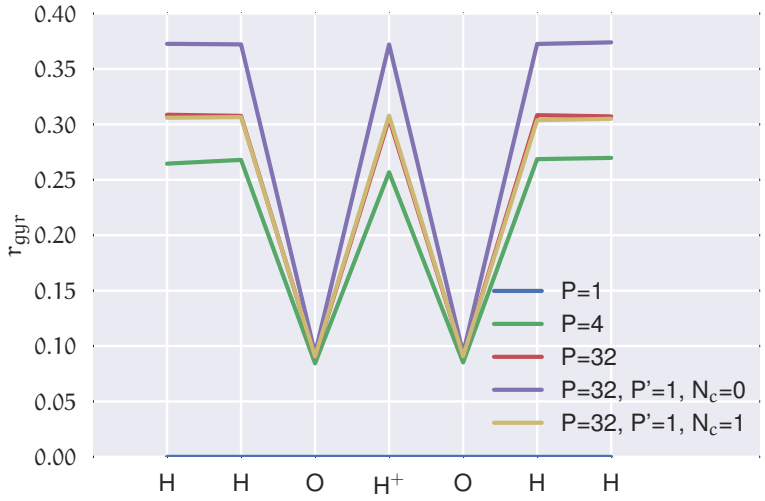

Figure 6.6: Mean gyration radius of the atoms in the protonated water dimer in the CC-PIMD simulation and different approximations to the quantum molecular dynamics simulation.

distances, where the harmonic approximation can be better assumed. Only for long distances the force is approximately constant on the size of the ring polymer and the fully converged result is retained. The converged quantum simulation is somewhere in between both of these possible approaches so far. Using a higher value of P' to not only converge to the centroid, shows that the PCF is converging also to the correct result in the limit of $P' = P$. A quantum thermostat includes quantum fluctuations to the classical nuclei with $P = 1$ and therefore approximates the mean fluctuations in all spatial dimensions with a colored-noise, generalized Langevin equation (GLE [141, 142]). Thereby, only the harmonic contribution of the nuclear quantum effects are included in the simulations so that the biggest fraction of the quantum change is included in the O–H PCF in Fig. 6.4b. The full capability of the extended ring polymer contraction can already be seen within the harmonic limit of the Taylor polynomial, i.e. $N_c = 1$. As depicted in Fig. 6.4b, the forces acting on the particles are dramatically corrected when the oxygen and hydrogens are approaching each other and the radius of gyration of all particles is almost the same as in the full $P = 32$ simulation as shown in Fig. 6.6. This demonstrates that also anharmonic nuclear quantum effects are taken into account despite being in the harmonic limit, because the correction of the second derivative in Eq. 6.6 is proportional to the distance of the beads from the centroid. This proportionality

includes the anharmonic portion that is also corrected with this approach. Now the force and the radius of gyrations of the expanded ring polymer are approximately the same than the fully converged simulation with $P = 32$ and in each time step only one calculation of the force and hessian needs to be done instead of 32 times a force calculation. Due to the computational more complex calculation of the analytic second derivatives, the total saved computational effort is only about a factor of two. At lower temperatures, when an huge number of beads is necessary such as in the previous Chapter 5, a bigger fraction of computational time can be saved.

6.3 CONCLUSIONS

In this chapter, the extended ring contraction scheme with further derivatives was shown to be a reasonable and sound improvement of the standard ring polymer contraction scheme by Markland *et al.* [45, 46]. Furthermore, this approach provides a systematic way to incorporate nuclear quantum effects that can be applied to any analytic potential. It has further the advantage that calculations of the energy (and derivatives thereof) are only carried out on the contracted ring polymer and no calculation on the full bead system is required. This is especially useful at low temperatures, where the number of beads P is steadily increasing and any calculation — even approximate ones at a lower level of theory fields such as in Chapter 5 — will sum up to yield a significant computational cost and limits the maximum number of beads P that can be carried out at maximum.

Part IV

CONCLUSIONS

7

CONCLUSIONS AND OUTLOOK

The key topic of this thesis was to advance the field of computational chemistry by combining highly accurate coupled cluster methods with path integral molecular dynamics, which was christened as *quantum molecular dynamics*. This approach includes quantum effects arising from electronic motions as well as finitely delocalized nuclei in an highly accurate and systematic way at finite temperatures. Both effects play a crucial role for a precise qualitative and quantitative simulation especially of light atoms such as in Chapter 5 or strong double bonds such as in Chapter 4. Furthermore, the efficient approximations of the coupled cluster methods as well as new approaches to reduce the computational effort of the path integral formalism were presented. In the following a summary of the results is given together with an outlook on future development.

In Part II, the first path integral molecular dynamics simulations with a coupled cluster based interatomic potential have been carried out, which can now be routinely applied. These is to the best of our knowledge the first molecular dynamics simulation at the coupled cluster level of theory and the first coupled cluster-based *ab initio* path integral molecular dynamics simulation ever realized. In Chapter 3, the molecular orbitals from the previous time steps have been used to estimate the solution of the self-consistent field equations at the next time step. This decreases the number of iterations needed to converge to the ground state and has sped up the Hartree-Fock part of the calculations. For the extrapolation, the always stable predictor by Kolafa [88] has been employed, which is in the same spirit as the second generation Car-Parrinello approach by Kühne *et al.* [43]. In coupled cluster, there are also iterative equations to calculate the energy and derivatives of the energy. In Chapter 4, the time to solve those equations has been reduced greatly by providing a good initial guess to the cluster and $\hat{\Lambda}$ amplitude equations. In order to do that, the corresponding amplitudes have been transformed to an intermediate

representation which approximately incorporates unitary transformations between successive molecular orbitals so that those amplitudes can be better extrapolated in time. Moreover, an approximate solution of the cluster amplitudes achieved by iterating the cluster equations only twice introduced barely visible deviations from the fully converged solution and is advised for further applications. In the case of an asymmetric proton system, consisting of a proton bound between a water molecule and a formaldehyde molecule, the computational cost was reduced by about 38.8% with this new approach and allowed for unambiguous quantification of the contribution of finite temperatures by comparing the ensemble averages of the path integral molecular dynamics trajectory with the molecular dynamics ensemble averages. It has been shown that the electronic as well as nuclei quantum effects were absolutely necessary to describe the asymmetric bonding of the proton. The structural change induced by the correct treatment of the additional quantum degrees of freedom due to nuclear quantum effects has been closely investigated by nuclear magnetic shielding tensor calculations and compared to the symmetric proton environment of the protonated water dimer from Chapter 3.

In Part III, new methods that can be applied to general path integral molecular dynamics simulations have been presented. In Chapter 5, the *ab initio* interatomic potential of the ring polymer is decomposed to an approximate and computational favorable potential at a lower level of theory and the difference of the lower level of theory and the full calculation. Coincidentally, these two parts consist of the Hartree-Fock and correlation contribution to the total interatomic potential. It has been shown that the computationally demanding correlation contribution can be approximated efficiently on a smaller, contracted ring polymer with the standard ring contraction scheme by Markland *et al.* [45, 46]. This decomposition of the interatomic potential was directly used as a fast and slowly varying part in an integration scheme with multiple time steps which was derived with the Liouville formalism. To our knowledge, this is the first simulation that combines a ring contraction scheme with a multiple time step algorithm. For the case of the computationally very demanding path integral molecular dynamics simulation of H_5^+ at low temperatures high number of beads were necessary. The correlation effects of both, the electronic and the quantum nuclear degrees of freedom were found to be of enormous importance and need to be carefully and accurately sampled to correctly describe the system qualitatively and quantitatively. With the clever use of the ring contraction scheme, a theoretical speed-up of a factor of 9.6 was achieved,

when the Hartree-Fock calculation is assumed to be of negligible computational cost. The multiple time step algorithm saved another factor of five of computational resources, which multiplies to a total theoretical speed-up factor of 48. As in practice the computational demands of the Hartree-Fock calculations is about a quarter of the one of the coupled cluster calculations, at maximum a speed-up of four can be achieved [140]. The real total speed-up that was achieved with this new approach was a factor of 3.6, which is 90% of the maximum possible one. In the classical molecular dynamics simulation, the investigated H_5^+ system was found almost at the ground state of a geometric optimization with a H_2 dimer and a separated H_3^+ trimer. Yet in the quantum simulation the light hydrogens undergo extreme excursions and the proton in the middle is fully delocalized. In Chapter 6, the standard ring contraction scheme was extended to include further derivatives of the analytic interatomic potential. It was shown that other established path integral methods are contained within this new scheme and it is therefore a reasonable and sound improvement that consistently converges to the true quantum result. Furthermore, this new approach to incorporate nuclear quantum effects in a systematic way with derivatives can be applied to any analytic potential. Yet in this thesis, it was carried out consistently on the coupled cluster level of theory. This yields the advantage that calculations of the energy (and derivatives thereof) are only carried out on the contracted ring polymer and no calculation on the full bead system is required. This is especially useful at low temperatures, where the number of beads P is steadily increasing and any calculation — even approximate ones at a lower level of theory such as in Chapter 5 — will sum up to yield a significant computational cost and limits the maximum possible speed-up as shown above. This new approach was benchmarked against the reference calculations of the protonated water dimer already carried out in Chapter 3. Analytic second derivatives of the centroid sufficed to yield the approximate quantum result. Nevertheless, this approach saved about a factor of two of computational cost due to the computational complexity of the analytic second derivatives of the coupled cluster theory.

In conclusion a fast and versatile computational method was developed that allows to access systems with greater accuracy than established methods. Its transferability should allow it to enhance studies of systems where a great level of accuracy and dynamics is desirable, such as systems with light atoms at finite temperature.

In the future, all of those three methods can be further developed and extended to bigger systems. For instance, the ring contraction schemes showed a particularity when the radius of gyration of the particles are bigger than a typical bond length. In that case the atoms of the contracted ring polymer approach too close, so that the delta potential cannot be efficiently calculated any more. As the centroid density has no physical meaning [136–139], this can not be easily circumvented and a different contraction scheme needs to be invented to contract to an even lower number of beads, where the interatomic potential can be determined. This would be especially useful at low temperatures, as in this work only a contracted ring polymer with $P' = 20$ could be used in the case of H_5^+ in Chapter 5. There is a more concrete plan for the future development of the transformation and extrapolation method of the cluster and $\hat{\Lambda}$ amplitudes. This new approach would reduce the computational demands even more by applying this approach to the amplitudes of density fitted coupled cluster [125] as it has the advantage that the memory limiting integrals are not calculated and saved to disk like in the current simulation but estimated with an auxiliary basis set on the fly. Then, less computational time would be spend in the integral evaluation and the transformation and extrapolation scheme may save an ever bigger fraction of the computational cost of future simulations and will make new applications for bigger systems possible.

LIST OF FIGURES

CODE LISTINGS

BIBLIOGRAPHY

[1] Melodysheep, *Symphony of science - the quantum world!*, https://www.youtube.com/watch?v=DZGINaRUEkU (2011), accessed: 2015-08-07.

[2] D. Chandler, *Exploiting the isomorphism between quantum theory and classical statistical mechanics of polyatomic fluids*, *J. Chem. Phys.*, **74**, 4078 (1981).

[3] M. Parrinello and A. Rahman, *Study of an F center in molten KCl*, *J. Chem. Phys.*, **80**, 860 (1984).

[4] I. R. Craig and D. E. Manolopoulos, *Quantum statistics and classical mechanics: Real time correlation functions from ring polymer molecular dynamics*, *J. Chem. Phys.*, **121**, 3368 (2004).

[5] D. M. Ceperley, *Path integrals in the theory of condensed helium*, *Rev. Mod. Phys.*, **67**, 279 (1995).

[6] D. Marx and M. Parrinello, *Ab initio path integral molecular dynamics: Basic ideas*, *J. Chem. Phys.*, **104**, 4077 (1996).

[7] M. E. Tuckerman, D. Marx, M. L. Klein, and M. Parrinello, *Efficient and general algorithms for path integral Car–Parrinello molecular dynamic*, *J. Chem. Phys.*, **104**, 5579 (1996).

[8] M. Pavese, D. R. Berard, and G. A. Voth, *Ab initio centroid molecular dynamics: a fully quantum method for condensed-phase dynamics simulations*, *Chem. Phys. Lett.*, **300**, 93 (1999).

[9] M. Shiga, M. Tachikawa, and S. Miura, *A unified scheme for ab initio molecular orbital theory and path integral molecular dynamics*, *J. Chem. Phys.*, **115**, 9149 (2001).

[10] M. Shiga and A. Nakayama, *Ab initio path integral ring polymer molecular dynamics: Vibrational spectra of molecules*, *Chem. Phys. Lett.*, **451**, 175 (2008).

[11] D. Marx and M. Parrinello, *Structural quantum effects and three-centre two-electron bonding in CH_5^+*, *Nature*, **375**, 216 (1995).

[12] M. E. Tuckerman, D. Marx, M. L. Klein, and M. Parrinello, *On the quantum nature of the shared proton in hydrogen bonds*, *Science*, **275**, 817 (1997).

[13] R. O. Weht, J. Kohanoff, D. A. Estrin, and C. Chakravarty, *An ab initio path integral monte carlo simulation method for molecules and clusters: Application to Li_4 and Li_5^+*, *J. Chem. Phys.*, **108**, 8848 (1998).

[14] M. Benoit, D. Marx, and M. Parrinello, *Tunnelling and zero-point motion in high-pressure ice*, *Nature*, **392**, 258 (1998).

[15] H. S. Mei, M. E. Tuckerman, D. E. Sagnella, and M. L. Klein, *Quantum nuclear ab initio molecular dynamics study of water wires*, *J. Phys. Chem. B*, **102**, 10446 (1998).

[16] D. Marx, M. E. Tuckerman, J. Hutter, and M. Parrinello, *The nature of the hydrated excess proton in water*, *Nature*, **397**, 601 (1999).

[17] M. E. Tuckerman, D. Marx, and M. Parrinello, *The nature and transport mechanism of hydrated hydroxide ions in aqueous solution*, *Nature*, **417**, 925 (2002).

[18] D. Marx, *Proton transfer 200 years after von Grotthuss: Insights from ab initio simulations*, *Chem. Phys. Chem.*, **7**, 1848 (2006).

[19] J. Morrone and R. Car, *Nuclear quantum effects in water*, *Phys. Rev. Lett.*, **101** (2008).

[20] A. Kaczmarek, M. Shiga, and D. Marx, *Quantum Effects on Vibrational and Electronic Spectra of Hydrazine Studied by "On-the-Fly" ab Initio Ring Polymer Molecular Dynamics*, *J. Phys. Chem. A*, **113**, 1985 (2009).

[21] G. A. Ludueña, M. Wegner, L. Bjålie, and D. Sebastiani, *Local disorder in hydrogen storage compounds: The case of lithium amide/imide*, *Chem. Eur. J. of Chem. Phys.*, **11**, 2353 (2010).

[22] M. Shiga, K. Suzuki, and M. Tachikawa, *The chemical shift of deprotonated water dimer: Ab initio path integral simulation*, *J. Chem. Phys.*, **132**, 114104 (2010).

[23] X.-Z. Li, B. Walker, and A. Michaelides, *Quantum nature of the hydrogen bond*, *Proc. Nat. Acad. Sci. USA*, **108**, 6369 (2011).

[24] V. Srinivasan and D. Sebastiani, *The isotope-effect in the phase transition of KH_2PO_4: New insights from ab initio path-integral simulations*, *J. Phys. Chem. C*, **115**, 12631 (2011).

[25] R. L. Hayes, S. J. Paddison, and M. E. Tuckerman, *Proton transport in triflic acid pentahydrate studied via ab initio path integral molecular dynamics*, *J. Phys. Chem. A*, **115**, 6112 (2011).

[26] M. Ceriotti, J. Cuny, M. Parrinello, and D. E. Manolopoulos, *Nuclear quantum effects and hydrogen bond fluctuations in water*, *Proc. Nat. Acad. Sci. USA*, **110**, 15591 (2013).

[27] O. Svoboda, D. Hollas, M. Ončák, and P. Slavíček, *Reaction selectivity in an ionized water dimer: nonadiabatic ab initio dynamics simulations*, *Phys. Chem. Chem. Phys.*, **15**, 11531 (2013).

[28] M. Dračínský and P. Hodgkinson, *Effects of quantum nuclear delocalisation on nmr parameters from path integral molecular dynamics*, *Chem. Eur. J.*, **20**, 2201 (2014).

[29] R. O. Jones and O. Gunnarsson, *The density functional formalism, its applications and prospects*, *Rev. Mod. Phys.*, **61**, 689 (1989).

[30] W. Kohn, *Nobel lecture: Electronic structure of matter—wave functions and density functionals*, *Rev. Mod. Phys.*, **71**, 1253 (1999).

[31] R. Van Noorden, B. Maher, and R. Nuzzo, *The top 100 papers*, *Nature*, **514**, 550 (2014).

[32] T. D. Kühne and R. Z. Khaliullin, *Electronic signature of the instantaneous asymmetry in the first coordination shell of liquid water*, *Nature Communications*, **4**, 1450 (2013).

[33] R. Z. Khaliullin and T. D. Kühne, *Microscopic properties of liquid water from combined ab initio molecular dynamics and energy decomposition studies*, *Phys. Chem. Chem. Phys.*, **15**, 15746 (2013).

[34] T. D. Kühne and R. Z. Khaliullin, *Nature of the asymmetry in the hydrogen-bond networks of hexagonal ice and liquid water*, *J. Am. Chem. Soc.*, **136**, 3395 (2014).

[35] M. Parrinello, *From silicon to RNA: The coming of age of ab initio molecular dynamics*, *Solid State Commun.*, **102**, 107 (1997).

[36] T. D. Kühne, M. Krack, and M. Parrinello, *Static and Dynamical Properties of Liquid Water from First Principles by a Novel Car- Parrinello-like Approach*, *J. Chem. Theory Comput.*, **5**, 235 (2009).

[37] T. Spura, H. Elgabarty, and T. D. Kühne, *"On-the-fly" coupled cluster path-integral molecular dynamics: Impact of nuclear quantum effects on the protonated water dimer*, *Phys. Chem. Chem. Phys.*, **17**, 14355 (2015).

[38] J. A. Pople, *Quantum chemical models (nobel lecture)*, *Angewandte Chemie International Edition*, **38**, 1894 (1999).

[39] T. Helgaker, J. Olsen, and P. Jørgensen, *Molecular Electronic-Structure Theory*, John Wiley & Sons, Chichster (2000).

[40] J. Čížek, *On the correlation problem in atomic and molecular systems. calculation of wavefunction components in ursell-type expansion using quantum-field theoretical methods*, *J. Chem. Phys.*, **45**, 4256 (1966).

[41] J. Gauss, *Coupled-cluster theory*, in P. v. R. Schleyer, editor, *Encyclopedia of Computational Chemistry*, vol. 1, pages 615–636, Wiley, Chichster (1998).

[42] R. J. Bartlett and M. Musiał, *Coupled-cluster theory in quantum chemistry*, *Rev. Mod. Phys.*, **79**, 291 (2007).

[43] T. Kühne, M. Krack, F. Mohamed, and M. Parrinello, *Efficient and accurate car-parrinello-like approach to born-oppenheimer molecular dynamics*, *Phys. Rev. Lett.*, **98**, 066401 (2007).

[44] T. D. Kühne, *Second generation car-parrinello molecular dynamics*, *WIREs: Comput. Mol. Sci.*, **4**, 391 (2014).

[45] T. E. Markland and D. E. Manolopoulos, *A refined ring polymer contraction scheme for systems with electrostatic interactions*, *Chem. Phys. Lett.*, **464**, 256 (2008).

[46] T. E. Markland and D. E. Manolopoulos, *An efficient ring polymer contraction scheme for imaginary time path integral simulations*, *J. Chem. Phys.*, **129**, 024105 (2008).

[47] T. Spura, H. Elgabarty, and T. D. Kühne, *Accelerated "on-the-fly" coupled cluster path-integral molecular dynamics: Impact of nuclear quantum effects on an asymmetric proton*, *in preparation* (2015).

[48] T. Spura, H. Elgabarty, and T. D. Kühne, *Quantum ring contraction scheme with a delta potential: Impact of nuclear quantum effects on H_5^+*, *in preparation* (2015).

[49] T. Spura and T. D. Kühne, *Quantum ring contraction scheme with derivatives*, *in preparation* (2015).

[50] M. Doemer, T. Spura, R. Z. Khaliullin, and T. D. Kuehne, *Tetrahedral, when in fluid state*, *Nachr. Chem.*, **61**, 1203 (2013).

[51] T. Spura, C. John, S. Habershon, and T. D. Kühne, *Nuclear quantum effects in liquid water from path-integral simulations using an ab initio force-matching approach*, *Mol. Phys.*, **113**, 808 (2014).

[52] J. Kessler, H. Elgabarty, T. Spura, K. Karhan, P. Partovi-Azar, A. A. Hassanali, and T. D. Kühne, *Structure and dynamics of the instantaneous water/vapor interface revisited by path-integral and ab initio molecular dynamics simulations*, *J. Phys. Chem. B*, **119**, 10079 (2015).

[53] T. Spura, P. Virnau, and T. D. Kühne, *High precision estimates of liquid-vapor critical points for water-salt mixtures*, *in preparation* (2015).

[54] A. Köster, T. Spura, G. Rutkai, H. Wiebeler, T. D. Kühne, and J. Vrabec, *Thermodynamic properties of force-matched water force fields*, *in preparation* (2015).

[55] H. Wiebeler, T. Spura, and T. D. Kühne, *Nuclear quantum effects in liquid water with three body corrected, path integral simulations*, *in preparation* (2015).

[56] C. John, T. Spura, J. Kessler, S. Habershon, and T. D. Kühne, *An auxillary potential ring-polymer contraction scheme for path integral molecular dynamics simulations*, *in preparation* (2015).

[57] M. E. Tuckerman, *Statistical mechanics: theory and molecular simulation*, Oxford University Press, USA (2010).

[58] M. Tuckerman, B. J. Berne, and G. J. Martyna, *Reversible multiple time scale molecular dynamics*, *J. Chem. Phys.*, **97**, 1990 (1992).

[59] L. Verlet, *Computer "Experiments" on Classical Fluids. I. Thermodynamical Properties of Lennard-Jones Molecules*, *Phys. Rev.*, **159**, 98 (1967).

[60] W. Swope, H. Andersen, P. Berens, and K. Wilson, *A computer simulation method for the calculation of equilibrium constants for the formation of physical clusters of molecules: Application to small water clusters*, *J. Chem. Phys.*, **76**, 637 (1982).

[61] D. Frenkel and B. Smit, *Understanding Molecular Simulation*, Academic Press, San Diego, second ed. (2002).

[62] H. F. Trotter, *On the product of semi-groups of operators*, *Proceedings of the American Mathematical Society*, **10**, 545 (1959).

[63] G. Strang, *On the construction and comparison of difference schemes*, *SIAM Journal on Numerical Analysis*, **5**, 506 (1968).

[64] H. De Raedt and B. De Raedt, *Applications of the generalized trotter formula*, *Phys. Rev. A*, **28**, 3575 (1983).

[65] M. E. Tuckerman and M. Parrinello, *Integrating the car–parrinello equations. ii. multiple time scale techniques*, *J. Chem. Phys.*, **101**, 1316 (1994).

[66] G. J. Martyna, M. E. Tuckerman, D. J. Tobias, and M. L. Klein, *Explicit reversible integrators for extended systems dynamics*, *Mol. Phys.*, **87**, 1117 (1996).

[67] N. Luehr, T. E. Markland, and T. J. Martínez, *Multiple time step integrators in ab initio molecular dynamics*, *J. Chem. Phys.*, **140**, 084116 (2014).

[68] M. Guidon, F. Schiffmann, J. Hutter, and J. VandeVondele, *Ab initio molecular dynamics using hybrid density functionals*, *J. Chem. Phys.*, **128**, 214104 (2008).

[69] R. P. Feynman and A. Hibbs, *Quantum Mechanics and Path Integrals*, McGraw-Hill, New York (1965).

[70] S. Habershon, D. E. Manolopoulos, T. E. Markland, and T. F. Miller, *Ring-polymer molecular dynamics: Quantum effects in chemical dynamics from classical trajectories in an extended phase space*, *Annu. Rev. Phys. Chem.*, **64**, 387 (2013).

[71] N. Makri and W. H. Miller, *Exponential power series expansion for the quantum time evolution operator*, *J. Chem. Phys.*, **90**, 904 (1989).

[72] M. E. Tuckerman, *Path integration via molecular dynamics*, in J. Grotendorst, D. Marx, and A. Muramatsu, editors, *Quantum Simulations of Complex Many-Body Systems: From Theory to Algorithms*, vol. 10, pages 269–298, NIC, FZ Jülich (2002).

[73] A. Szabo and N. S. Ostlund, *Modern quantum chemistry: Introduction to advanced electronic structure theory. revised*, *McGraw-Hili, New York* (1989).

[74] T. Helgaker, M. Jaszuński, and K. Ruud, *Ab initio methods for the calculation of NMR shielding and indirect spin–spin coupling constants*, *Chem. Rev.*, **99**, 293 (1999).

[75] J. C. Slater, *The theory of complex spectra*, *Phys. Rev.*, **34**, 1293 (1929).

[76] M. Hanrath, *On the concepts of connectivity, separability, and consistency: An illustration by partitioned diagrams and numerical probing*, *Chem. Phys.*, **356**, 31 (2009).

[77] R. J. Bartlett and G. D. Purvis, *Many-body perturbation theory, coupled-pair many-electron theory, and the importance of quadruple excitations for the correlation problem*, *Int. J. Quantum Chem.*, **14**, 561 (1978).

[78] L. Adamowicz, W. D. Laidig, and R. J. Bartlett, *Analytical gradients for the coupled-cluster method*, *Int. J. Quantum Chem.*, **26**, 245 (1984).

[79] H. Koch and P. Jørgensen, *Coupled cluster response functions*, *J. Chem. Phys.*, **93**, 3333 (1990).

[80] P. Szalay, *Analytic energy derivatives for coupled-cluster methods describing excited states: General formulas and comparison of computational costs*, *Int. J. Quantum Chem.*, **55**, 151 (1995).

[81] J. Arponen, *Variational principles and linked-cluster exp s expansions for static and dynamic many-body problems*, *Annals of Physics*, **151**, 311 (1983).

[82] K. Raghavachari, G. W. Trucks, J. A. Pople, and M. Head-Gordon, *A fifth-order perturbation comparison of electron correlation theories*, *Chem. Phys. Lett.*, **157**, 479 (1989).

[83] R. J. Bartlett, J. Watts, S. Kucharski, and J. Noga, *Non-iterative fifth-order triple and quadruple excitation energy corrections in correlated methods*, *Chem. Phys. Lett.*, **165**, 513 (1990).

[84] J. F. Stanton, *Why CCSD(T) works: a different perspective*, *Chem. Phys. Lett.*, **281**, 130 (1997).

[85] W. Humphrey, A. Dalke, and K. Schulten, *VMD – Visual Molecular Dynamics*, *J. Mol. Graph.*, **14**, 33 (1996).

[86] J. Sauer and J. Döbler, *Gas-phase infrared spectrum of the protonated water dimer: Molecular dynamics simulation and accuracy of the potential energy surface*, *Chem. Phys. Chem.*, **6**, 1706 (2005).

[87] S. Lammers and M. Meuwly, *Investigating the relationship between infrared spectra of shared protons in different chemical environments: A comparison of protonated diglyme and protonated water dimer*, *J. Phys. Chem. A*, **111**, 1638 (2007).

[88] J. Kolafa, *Time-reversible always stable predictor-corrector method for molecular dynamics of polarizable molecules*, *J. Comput. Chem.*, **25**, 335 (2004).

[89] J. Kolafa and M. Lısal, *Time-reversible velocity predictors for verlet integration with velocity-dependent right-hand side*, *J. Chem. Theory Comput.*, **7**, 3596 (2011).

[90] D. Richters and T. D. Kühne, *Self-consistent field theory based molecular dynamics with linear system-size scaling*, *J. Chem. Phys.*, **140**, 134109 (2014).

[91] T. H. Dunning, *Gaussian basis sets for use in correlated molecular calculations. i. the atoms boron through neon and hydrogen*, *J. Chem. Phys.*, **90**, 1007 (1989).

[92] M. Ceriotti, J. More, and D. E. Manolopoulos, *i-pi: A python interface for ab initio path integral molecular dynamics simulations*, *Comp. Phys. Comm.*, **185**, 1019 (2014).

[93] A. C. Scheiner, G. E. Scuseria, J. E. Rice, T. J. Lee, and H. F. Schaefer, *Analytic evaluation of energy gradients for the single and double excitation coupled cluster (CCSD) wave function: Theory and application*, *J. Chem. Phys.*, **87**, 5361 (1987).

[94] J. F. Stanton, J. Gauss, J. D. Watts, and R. J. Bartlett, *A direct product decomposition approach for symmetry exploitation in many-body methods. i. energy calculations*, *J. Chem. Phys.*, **94**, 4334 (1991).

[95] J. Gauss, J. F. Stanton, and R. J. Bartlett, *Coupled-cluster open-shell analytic gradients: Implementation of the direct product decomposition approach in energy gradient calculations*, *J. Chem. Phys.*, **95**, 2623 (1991).

[96] J. Gauss, W. J. Lauderdale, J. F. Stanton, J. D. Watts, and R. J. Bartlett, *Analytic energy gradients for open-shell coupled-cluster singles and doubles (CCSD) calculations using restricted open-shell hartree-fock (ROHF) reference functions*, *Chem. Phys. Lett.*, **182**, 207 (1991).

[97] M. E. Harding, T. Metzroth, J. Gauss, and A. A. Auer, *Parallel calculation of CCSD and CCSD(T) analytic first and second derivatives*, *J. Chem. Theory Comput.*, **4**, 64 (2008).

[98] J. F. Stanton, J. Gauss, M. E. Harding, P. Szalay, A. Auer, R. J. Bartlett, U. Benedikt, C. Berger, D. Bernholdt, Y. Bomble, et al., *CFOUR, a quantum chemical program package*, *For the current version, see http://www.cfour.de* (2011).

[99] J. Gauss and J. F. Stanton, *Perturbative treatment of triple excitations in coupled-cluster calculations of nuclear magnetic shielding constants*, *J. Chem. Phys.*, **104**, 2574 (1996).

[100] J. Gauss and J. F. Stanton, *Electron-correlated methods for the calculation of NMR chemical shifts*, in M. Kaupp, M. Bühl, and V. Malkin, editors, *Calculation of NMR and EPR Parameters: Theory and Applications*, page 123, Wiley-VCH, Weinheim (2004).

[101] E. F. Valeev and H. F. Schaefer, *The protonated water dimer: Brueckner methods remove the spurious C_1 symmetry minimum*, *J. Chem. Phys.*, **108**, 7197 (1998).

[102] A. A. Auer, T. Helgaker, and W. Klopper, *Accurate molecular geometries of the protonated water dimer*, *Phys. Chem. Chem. Phys.*, **2**, 2235 (2000).

[103] M. Dagrada, M. Casula, A. M. Saitta, S. Sorella, and F. Mauri, *Quantum Monte Carlo study of the protonated water dimer*, *J. Chem. Theory Comput.*, **10**, 1980 (2014).

[104] J. E. Del Bene, S. A. Perera, and R. J. Bartlett, *Hydrogen bond types, binding energies, and ^1H nmr chemical shifts*, *J. Phys. Chem. A*, **103**, 8121 (1999).

[105] A. L. Sobolewski and W. Domcke, *Ab initio investigation of the structure and spectroscopy of hydronium—water clusters*, *J. Phys. Chem. A*, **106**, 4158 (2002).

[106] H.-H. Limbach, P. M. Tolstoy, N. Pérez-Hernández, J. Guo, I. G. Shenderovich, and G. S. Denisov, *OHO hydrogen bond geometries and NMR chemical shifts: From*

equilibrium structures to geometric H/D isotope effects, with applications for water, protonated water, and compressed ice, *Isr. J. Chem.*, **49**, 199 (2009).

[107] T. Spura, H. Elgabarty, and T. D. Kühne, *Correction: "On-the-fly" coupled cluster path-integral molecular dynamics: Impact of nuclear quantum effects on the protonated water dimer*, *Phys. Chem. Chem. Phys.*, **17**, 19673 (2015).

[108] A. A. Hassanali, J. Cuny, M. Ceriotti, C. J. Pickard, and M. Parrinello, *The fuzzy quantum proton in the hydrogen chloride hydrates*, *J. Am. Chem. Soc.*, **134**, 8557 (2012).

[109] J. S. Waugh, L. M. Huber, and U. Haeberlen, *Approach to high-resolution nmr in solids*, *Phys. Rev. Lett.*, **20**, 180 (1968).

[110] S. G. Kukolich, *Proton magnetic shielding tensors from spin-rotation measurements on formaldehyde and ammonia*, *J. Am. Chem. Soc.*, **97**, 5704 (1975).

[111] F. Schönborn, H. Schmitt, H. Zimmermann, U. Haeberlen, C. Corminboeuf, G. Großmann, and T. Heine, *The proton nuclear magnetic shielding tensors in biphenyl: Experiment and theory*, *J. Magn. Reson.*, **175**, 52 (2005).

[112] K. Modig and B. Halle, *Proton magnetic shielding tensor in liquid water*, *J. Am. Chem. Soc.*, **124**, 12031 (2002).

[113] P. Pulay, *Convergence acceleration of iterative sequences. The case of SCF iteration*, *Chem. Phys. Lett.*, **73**, 393 (1980).

[114] P. Pulay, *Improved SCF convergence acceleration*, *J. Comput. Chem.*, **3**, 556 (1982).

[115] J. M. Turney, A. C. Simmonett, R. M. Parrish, E. G. Hohenstein, F. A. Evangelista, J. T. Fermann, B. J. Mintz, L. A. Burns, J. J. Wilke, M. L. Abrams, and et al., *Psi4: an open-source ab initio electronic structure program*, *WIREs: Comput. Mol. Sci.*, **2**, 556 (2011).

[116] T. D. Crawford and H. F. Schaefer, *An introduction to coupled cluster theory for computational chemists*, *Rev. Comp. Chem.*, **14**, 33 (2000).

[117] J. D. Hunter, *Matplotlib: A 2d graphics environment*, *Computing In Science & Engineering*, **9**, 90 (2007).

[118] A. Grimmer, *Shielding tensor data and structure: the bond-related chemical shift concept*, in J. Tossell, editor, *Nuclear magnetic shieldings and molecular structure*, vol. 386, pages 191–201, Kluwer Academic Publishers, Dordrecht (1993).

[119] J. Vaara, J. Lounila, K. Ruud, and T. Helgaker, *Rovibrational effects, temperature dependence, and isotope effects on the nuclear shielding tensors of water: A new ^{17}O absolute shielding scale*, *J. Chem. Phys.*, **109**, 8388 (1998).

[120] M. Dračínský, J. Kaminský, and P. Bouř, *Relative importance of first and second derivatives of nuclear magnetic resonance chemical shifts and spin-spin coupling constants for vibrational averaging*, *J. Chem. Phys.*, **130**, 094106 (2009).

[121] M. C. Böhm, J. Schulte, and R. Ramírez, *On the influence of nuclear fluctuations on calculated NMR shieldings of benzene and ethylene: a Feynman path integral-ab initio investigation*, *Int. J. Quantum Chem.*, **86**, 280–296 (2001).

[122] J. Schulte, R. Ramírez, and M. C. Böhm, *Influence of nuclear fluctuations on the NMR parameters of bullvalene: A Feynman path integral – Ab initio study*, *Chem. Phys. Lett.*, **432**, 579–584 (2006).

[123] M. Dračínský and P. Hodgkinson, *Effects of Quantum Nuclear Delocalisation on NMR Parameters from Path Integral Molecular Dynamics*, *Chem. Eur. J.*, **20**, 2201 (2014).

[124] J. Gauss and J. F. Stanton, *Coupled-cluster calculations of nuclear magnetic resonance chemical shifts*, *J. Chem. Phys.*, **103**, 3561 (1995).

[125] A. E. DePrince and C. D. Sherrill, *Accuracy and efficiency of coupled-cluster theory using density fitting/cholesky decomposition, frozen natural orbitals, and a t_1-transformed hamiltonian*, *J. Chem. Theory Comput.*, **9**, 2687 (2013).

[126] E. Anglada, J. Junquera, and J. M. Soler, *Efficient mixed-force first-principles molecular dynamics*, *Phys. Rev. E*, **68** (2003).

[127] R. P. Steele, *Communication: Multiple-timestep ab initio molecular dynamics with electron correlation*, *J. Chem. Phys.*, **139**, 011102 (2013).

[128] M. Ceriotti, M. Parrinello, T. E. Markland, and D. E. Manolopoulos, *Efficient stochastic thermostatting of path integral molecular dynamics*, *J. Chem. Phys.*, **133**, 124104 (2010).

[129] J. D. Watts, J. Gauss, and R. J. Bartlett, *Coupled-cluster methods with noniterative triple excitations for restricted open-shell hartree–fock and other general single determinant reference functions. energies and analytical gradients*, *J. Chem. Phys.*, **98**, 8718 (1993).

[130] I. Štich, D. Marx, M. Parrinello, and K. Terakura, *Protonated hydrogen clusters*, *J. Chem. Phys.*, **107**, 9482 (1997).

[131] I. Štich, D. Marx, M. Parrinello, and K. Terakura, *Proton-induced plasticity in hydrogen clusters*, *Phys. Rev. Lett.*, **78**, 3669 (1997).

[132] M. Farizon, B. Farizon-Mazuy, N. de Castro Faria, and H. Chermette, *Ab initio structure calculations of hydrogen ionic clusters*, *Chem. Phys. Lett.*, **177**, 451 (1991).

[133] M. Farizon, H. Chermette, and B. Farizon-Mazuy, *Structure and energetics of hydrogen clusters. structures of H_{11}^+ and H_{13}^+ vibrational frequencies and infrared intensities of the H_{2n+1}^+ clusters $(n = 2-6)$*, *J. Chem. Phys.*, **96**, 1325 (1992).

[134] T. Pang, *Properties of ionic hydrogen clusters: a quantum Monte Carlo study*, *Chem. Phys. Lett.*, **228**, 555 (1994).

[135] Y. Yamaguchi, J. F. Gaw, and H. F. Schaefer, *Molecular clustering about a positive ion. structures, energetics, and vibrational frequencies of the protonated hydrogen clusters H_3^+, H_5^+, H_7^+, and H_9^+*, *J. Chem. Phys.*, **78**, 4074 (1983).

[136] J. Cao and G. A. Voth, *The formulation of quantum statistical mechanics based on the feynman path centroid density. i. equilibrium properties*, *J. Chem. Phys.*, **100**, 5093 (1994).

[137] J. Cao and G. A. Voth, *The formulation of quantum statistical mechanics based on the feynman path centroid density. ii. dynamical properties*, *J. Chem. Phys.*, **100**, 5106 (1994).

[138] J. Cao and G. A. Voth, *The formulation of quantum statistical mechanics based on the feynman path centroid density. iii. phase space formalism and analysis of centroid molecular dynamics*, *J. Chem. Phys.*, **101**, 6157 (1994).

[139] J. Cao and G. A. Voth, *The formulation of quantum statistical mechanics based on the feynman path centroid density. iv. algorithms for centroid molecular dynamics*, *J. Chem. Phys.*, **101**, 6168 (1994).

[140] G. M. Amdahl, *Validity of the single processor approach to achieving large scale computing capabilities*, *AFIPS Conf. Proc.*, **30**, 483 (1967).

[141] M. Ceriotti, G. Bussi, and M. Parrinello, *Nuclear quantum effects in solids using a colored-noise thermostat*, *Phys. Rev. Lett.*, **103**, 030603 (2009).

[142] M. Ceriotti, G. Bussi, and M. Parrinello, *Colored-noise thermostats à la carte*, *J. Chem. Theory Comput.*, **6**, 1170 (2010).

[143] J. A. Pople, R. Krishnan, H. B. Schlegel, and J. S. Binkley, *Derivative studies in hartree-fock and møller-plesset theories*, *Int. J. Quantum Chem.*, **16**, 225 (1979).

[144] H. Koch, H. J. A. Jensen, P. Jørgensen, T. Helgaker, G. E. Scuseria, and H. F. Schaefer, *Coupled cluster energy derivatives. analytic hessian for the closed-shell coupled cluster singles and doubles wave function: Theory and applications*, *J. Chem. Phys.*, **92**, 4924 (1990).

[145] P. Szalay, J. Gauss, and J. F. Stanton, *Analytic UHF-CCSD(T) second derivatives: implementation and application to the calculation of the vibration-rotation interaction constants of NCO and NCS*, *Theor. Chem. Acc.*, **100**, 5 (1998).

ACKNOWLEDGMENTS

This work was benefited by several colleagues and companions over the last years, whom I would like to thank for all their efforts.

Firstly, I would like to thank my adviser Prof. Dr. Thomas D. Kühne for having me as one of his first group members (at that time as student assistant) at the University of Mainz, where I could see his group growing and rising to an international and interdisciplinary environment. I thank him for his constant and tremendous support and numerous, fruitful and inspiring discussions.

Together with Kristof Karhan, Dr. Pouya Partovi-Azar and Hendrik Wiebeler, I joined the newly founded working group at the University of Paderborn. The former and present members of the working group in Mainz as well as in Paderborn created a pleasant and motivating environment with suggestions of various nature which helped tremendously while carrying out this work. In Paderborn, we were warmly welcomed by the Grundmeier group and in addition to that I would like to thank especially Christoph Ebbert, Chen-Ni Liu, Rabea Schreckenberg and Martin Wiesing for the great atmosphere and encouraging discussions.

I thank my closest co-worker Hossam Elgabarty whom with I enjoyed fruitful discussions of various nature such as topics ranging from basic chemistry to NMR or even the next football match.

Moreover, I thank Jun. Prof. Dr. Simone Sanna for investing time and effort in reviewing my thesis.

I owe a thank to Dr. Hans Behringer, Dr. Francesco Calcaveccia, Susanne Glienke, Dr. Stephan Köhler and Dr. Dorothea Wilms for critical reading of this work and helping with suggestions to clarify or rephrase some passages.

Lastly, I want to thank my family for their love and words of encouragement. My mother and my father for their constant support and I would not have made it this far without them. And especially my scientifically and morally supportive, loving and encouraging girlfriend Katharina.